SLAC PUB-15889
December 15, 2013

Measurements of Ionizing Radiation Doses Induced by High Irradiance Laser on Targets in LCLS MEC Instrument

J. Bauer, J. C. Liu, A. A. Prinz, S. Rokni, H. Tran, M. Woods, and Z. Xia
Radiation Protection Department

E. Galtier, H-J Lee, D. Milathianaki, B. Nagler
LCLS MEC and LSTD

SLAC National Accelerator Laboratory
2575 Sand Hill Road, Menlo Park, CA 94025

Abstract

Comprehensive measurements for photon and neutron radiation doses generated from laser-plasma interaction at SLAC's MEC laser facility have been conducted. The goals of the measurements were to:

1. determine the radiation dose per laser shot as a function of laser, optic and target parameters that are relevant to the MEC laser operations,
2. validate the RPD-developed analytic model for photon dose calculations, and
3. evaluate the performance of various types of passive and active detectors in the laser-induced radiation fields.

The MEC radiation measurements had laser irradiance between $3x10^{16}$ and $6x10^{17}$ W/cm^2 (about 30 to 150 mJ per pulse and 40 fs) hitting mainly thin gold and copper target plates. Radiation measurements with 10 Hz of laser pulses rastering over the target surface were conducted at various distances and angles relative to laser beam and target using a comprehensive set of passive and active detectors placed inside and outside the MEC aluminum target chamber, as well as outside the MEC hutch 6.

Both passive and active detectors measured photon doses that agree with the RPD dose model calculations in this irradiance range. Active detectors were not affected by the electromagnetic pulses associated with the laser operation.

Work supported in part by US Department of Energy under contract DE-AC02-76SF00515.

Introduction

It is known that high-power laser interaction with targets in vacuum at high laser irradiance levels can generate plasma and, consequently, create ionizing radiation hazards [1-4]. The theory for ionizing radiation generation from laser-plasma interaction is complicated. The basics of theory and phenomenology can be summarized qualitatively as follows [5,6]:

1. When a high-irradiance laser pulse hits a target, it can create plasma, and the subsequent laser-plasma interaction will produce "hot electrons" with a Maxwellian energy spectrum, characterized by the parameter called "electron temperature" for the spectral slope (the electron temperature ranges from about 10 to 10000 keV for irradiance between 10^{16} and 10^{21} W/cm^2),
2. Bremsstrahlung photons are produced when the hot electrons hit the target or surrounding materials (the higher the electron temperature, the higher the bremsstrahlung yield),
3. At 10^{19} W/cm^2 or above, production of protons and neutrons has been observed,
4. A gas target may generate higher radiation yield than a solid target, and
5. A laser with a higher pre-pulse or higher energy per pulse may generate higher radiation yields.

However, the ionizing radiation yields associated with laser-plasma interaction have not been well quantified. Based on the theoretical analysis and review of the published reports and measurement data [5,6], the Radiation Protection Department (RPD) at the SLAC National Accelerator Laboratory (SLAC) developed an analytic model to estimate conservatively the photon radiation yield (Sv per J) of a laser pulse hitting a solid target at 1 m.

In June 2011, RPD conducted radiation measurements at the LLNL Titan laser facility during laser induced plasma experiments, in which a laser beam of very high irradiance (~10^{20} W/cm^2) and high energy (up to 400 J per shot) hit a solid target (thick hydrocarbon foam and/or thin gold foil) [7]. The photon dose yields (about 0.01 to 1 mSv/J for 10^{20} to 10^{21} W/cm^2) measured at Titan were consistent with other published measurements and the maximum dose yields were about a factor of 10 below the doses estimated from the RPD model.

In March 2012, RPD worked with LCLS MEC Instrument and the SLAC Laser Science Technology Division (LSTD) to conduct an experiment to measure the photon and neutron radiation doses generated from laser-plasma interaction at SLAC's MEC laser facility. The experiment had laser irradiance between $3\text{x}10^{16}$ and $6\text{x}10^{17}$ W/cm^2 (40 fs and up to 0.15 J per pulse) hitting mainly thin gold and copper targets. These are the laser irradiance levels that MEC plans to operate currently and are also in a region where radiation measurement data for laser-plasma experiments are lacking.

The goals of the experiment were to: 1) determine the radiation dose per laser shot as a function of laser, optic and target parameters that are relevant to the MEC operations, 2) validate the RPD model for photon dose calculations, and 3) evaluate the performance of various types of passive and active detectors in the laser-induced radiation fields. The measurements also permitted to establish hazard analysis and safety control requirements for the MEC laser radiation hazard during later user experiments.

Because the neutron dose is a small fraction of the total dose at the anticipated MEC laser irradiance levels, the dose (or radiation) mentioned in this report refers to photon dose (or photon radiation) unless otherwise specifically stated.

Comprehensive radiation measurements around the MEC aluminum-wall target chamber were made at several irradiance levels. The laser and optic parameters were characterized to derive the irradiance values. Many different types of passive dosimeters and active detectors were placed inside and outside the target chamber to cover 4π directions relative to the laser beam direction. In this report, the methods and results for the characterization of laser/optic/target parameters and radiation dose measurements for MEC experiment are described.

MEC Laser and Optic Parameters and Experiment

This section defines the laser and optic parameters (laser energy per pulse, pulse length, optic focal length and spot size) for the derivation of irradiance, which is needed for the normalization of measured doses. The experimental conditions as well as the measurements of the laser, optic and target parameters during the experimental runs are also described.

Laser and Optic Parameters

The definitions of laser and optic parameters used in this report are described in a SLAC memo [8]. The radial irradiance (or intensity in W/cm^2) variation of a Gaussian laser beam is given by Eq. 1:

$$I(r) = \frac{2P}{\pi w^2} e^{-2r^2/w^2} \qquad (1)$$

The laser pulse peak power P (in watts) = E/t, where E is laser energy per pulse (in J) and t is laser pulse length (in seconds). The parameter w is the radius of the spot size, where the intensity has dropped to $1/e^2$ of its peak intensity. The effective diameter of a uniform cylindrical "top hat" beam with the same peak intensity and pulse energy is given in Eq. 2:

$$d_{TH} = \sqrt{2}w \qquad (2)$$

Figure 1 shows that when a collimated, incoming Gaussian laser beam (with wavelength λ and radial size w) is focused by an optic (with diameter D and focal length f), the focused beam will have a waist with radial spot size w_o, given by the diffraction limit, as shown in Eq. 3:

$$w_0 \approx \frac{f\lambda}{\pi w} = f^{\#}\lambda \qquad (3)$$

The f-number of a focusing optic is given by $f^{\#} = f/D$. The diameter D should be equal to πw or greater in order to transmit at least 99% of laser energy.

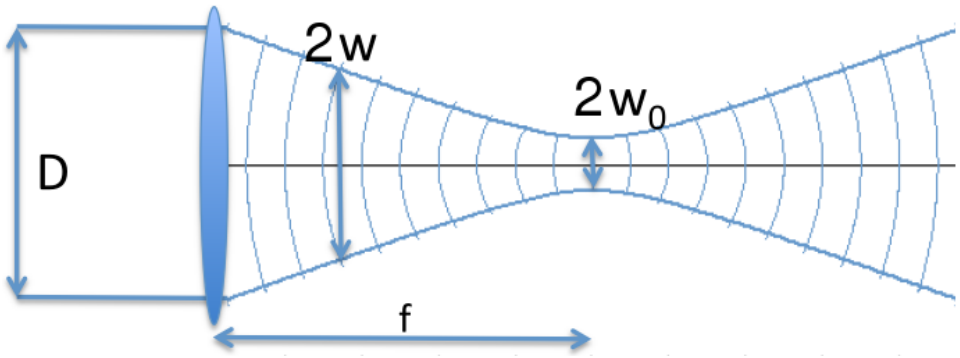

Figure 1: Focusing of a Gaussian beam to a waist with radial spot size w_o.

The peak irradiance (called irradiance or intensity hereafter) at the focus will then be given as Eq. 4:

$$I_0 = \frac{2P}{\pi w_0^2} \qquad (4)$$

Figure 2 gives a layout of the two MEC laser systems and the target chamber (about 1-m-radius and typically 2.54-cm-thick aluminum wall) in LCLS Hutch 6. Figure 3 sketches the short pulse (high peak power) and long pulse (low peak power) laser systems and lists their parameters. Since the long pulse system is unable to produce ionizing radiation, only the short pulse laser system was used for the dose measurements. See Figure 4 for the short pulse laser system components.

Figure 5 shows the MEC high power laser system with mirrors and focusing optic inside the target chamber. A range of laser irradiance (Eq. 4) on target was obtained by varying the focal spot size using the focusing optic, *e.g.*, by using a spherical mirror for low irradiance and the off-axis parabolic (OAP) mirror for high irradiance.

The MEC short pulse laser parameters are 0.8 μm wavelength, 150 mJ per pulse maximum energy, a pulse length (FWHM) of 40 fs minimum, and a repetition rate of 10 Hz maximum. With a minimum focal spot size w_o of 10 μm radius on the target (Gaussian beam assumed), the peak power P and maximum irradiance I_o for the MEC high power laser system are 3.75 TW and 2.4×10^{18} W/cm^2, respectively. Typical irradiance for current MEC user experiments using the short-pulse laser ranges from 10^{14} to 10^{18} W/cm^2.

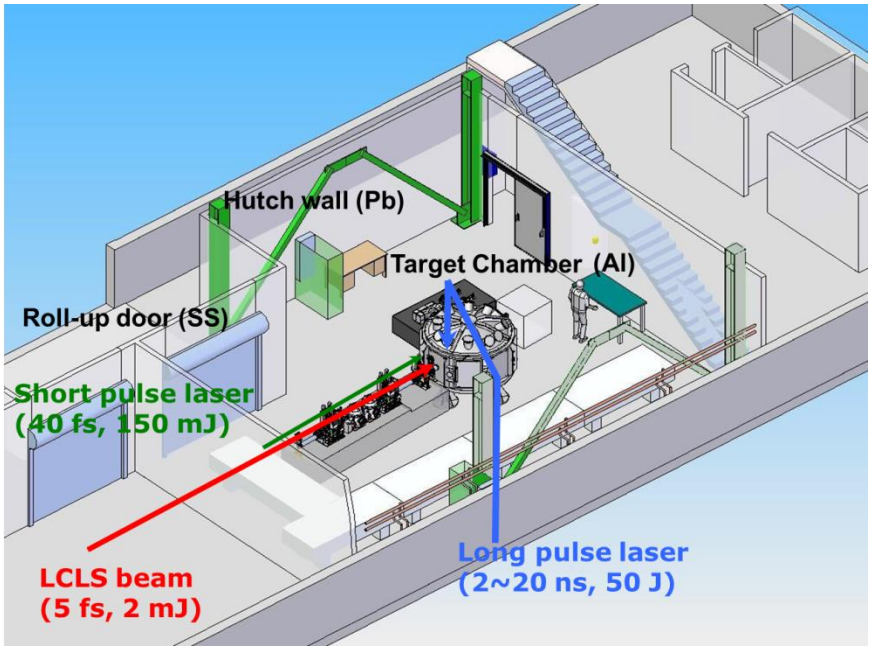

Figure 2: Layout of the target chamber (1-m-radius and aluminum wall) inside hutch 6, and short pulse and long pulse laser systems, for LCLS MEC Instrument.

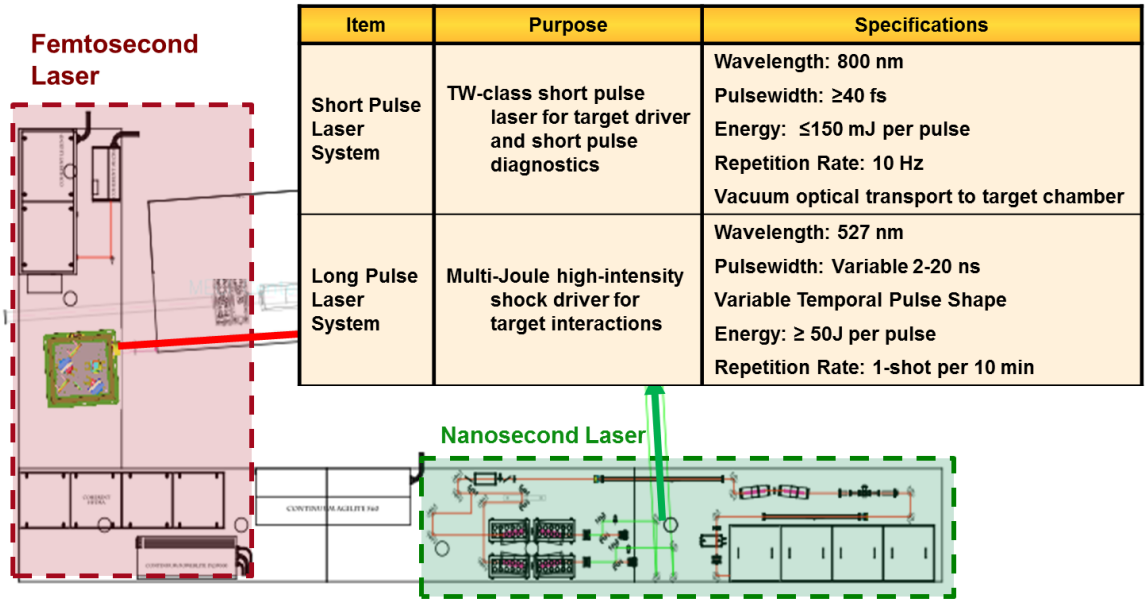

Item	Purpose	Specifications
Short Pulse Laser System	TW-class short pulse laser for target driver and short pulse diagnostics	Wavelength: 800 nm Pulsewidth: ≥40 fs Energy: ≤150 mJ per pulse Repetition Rate: 10 Hz Vacuum optical transport to target chamber
Long Pulse Laser System	Multi-Joule high-intensity shock driver for target interactions	Wavelength: 527 nm Pulsewidth: Variable 2-20 ns Variable Temporal Pulse Shape Energy: ≥ 50J per pulse Repetition Rate: 1-shot per 10 min

Figure 3: The short pulse and long pulse laser systems for MEC in Hutch 6.

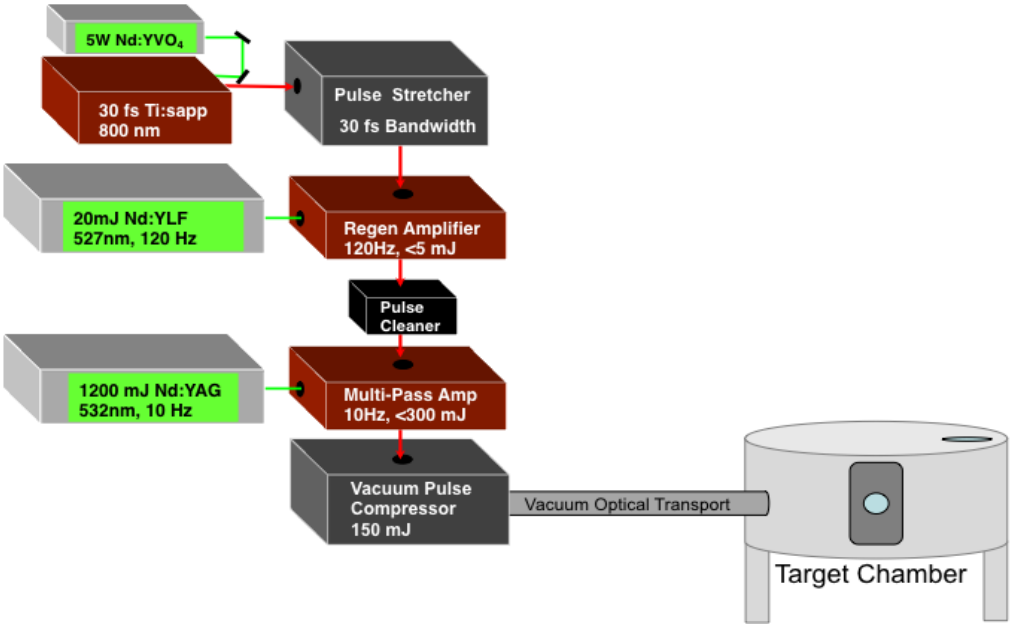

Figure 4: The MEC short pulse laser system components.

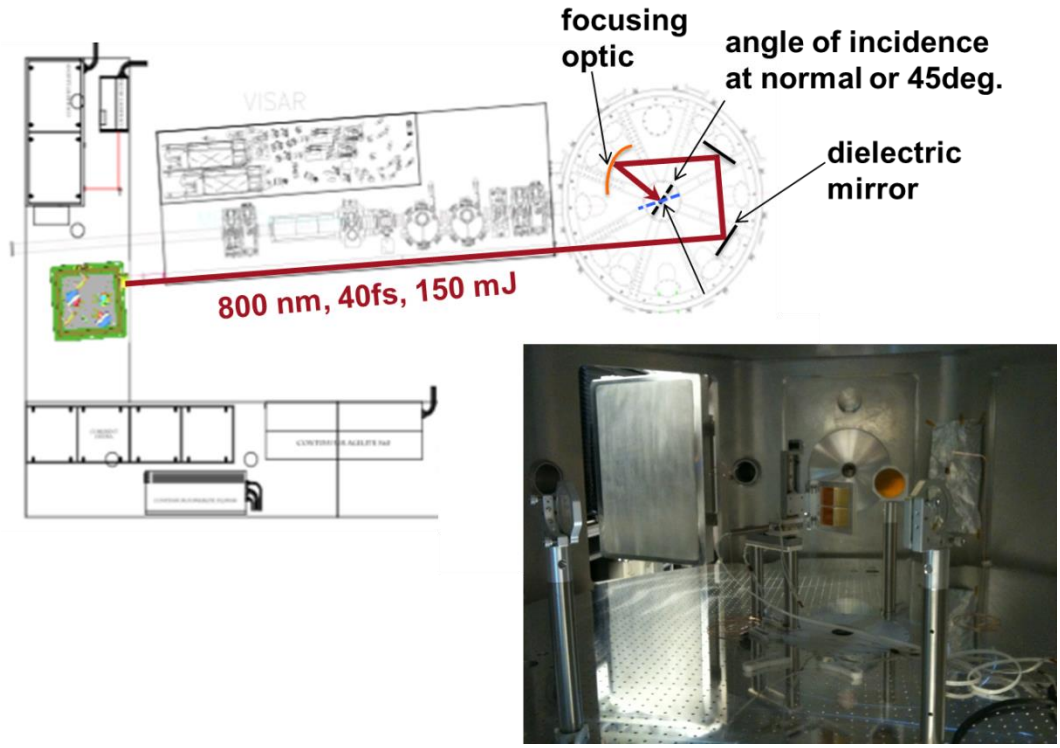

Figure 5: MEC high power laser system with typical focusing optics inside the target chamber.

Experiment and Characterization of Parameters

The radiation measurement experiment consisted of more than 20 runs, most of them with a unique set of laser, optic and target conditions. During each run, 10 Hz laser pulses were rastered over a target surface at a fixed irradiance. The laser irradiance values were measured for each configuration of laser, focusing mirror, and target. In the end, four laser irradiances (3.0×10^{16}, 5.2×10^{16}, 1.0×10^{17} and 6×10^{17} W/cm^2) from 10 runs were achieved to produce good results for the experiment. These ten runs at four irradiances will be referred to from now on to denote the runs with high-quality data.

The laser and optics parameters were measured before the experiment and monitored throughout the 10 runs at 4 irradiance values in the following manners (see also Table 1).

Laser Power

The laser energy hitting the target was characterized with the measurements below:

1. The laser energy before the compressor was measured with the Coherent J50 50M-YAG-1535 sensor and Coherent EPM2000 meter prior to the start of a new run and continuously monitored throughout the run via measurement of leakage through a dielectric mirror. The energy stayed stable at 210 to 220 mJ, measured with a 5% uncertainty (1σ).
2. Two laser energy loss factors were measured to account for the actual laser energy hitting the target:
    a. The transmission factor for the compressor optics was 0.65 (8% uncertainty), and
    b. The transmission factor from the reflectivity of the last focusing mirror was measured regularly. For spherical mirrors, this factor was found to be 100% both before and after the runs. For OAP mirrors, which were positioned closer to the target due to their shorter focus lengths, and therefore more susceptible to damage and coating, the transmission factor was 95% before the runs, but dropped to 37% to 60% after the runs.

The laser pulse length was characterized via Coherent Single Shot Autocorrelator (SSA) measurements. The measurement performed a few days before the experiment gave a pulse length of 40 fs. When the measurement was repeated a few weeks after the experiment, the result was 70 fs. This discrepancy was then used as uncertainty on the pulse length t (FWHM), which was therefore taken to be 55 ± 15 fs.

The laser pre-pulses were measured with contrast ratios for the pre-pulses around 10^5 to 10^6.

Spot Size

Equation 3 can be used to calculate the diffraction-limited beam size, which is the smallest achievable spot size in the setup. Since the beam was not a perfect Gaussian beam profile due to astigmatism, the actual focal spot size on the target surface (w_o) was measured from an attenuated beam.

For larger beam spots, a CCD camera (Spiricon-Ophir model SP620U, 4.4x4.4 μm pixel size, 1600x1200 pixels) was aligned directly in the focal plane using 3-dimensional manipulators. An image was then recorded and the spatial profile analyzed from the recorded image using the Spiricon-Ophir Beamgage software. This gave the 4-sigma diameter for both X and Y, $D_{4\sigma} = 2\ w_o$, where w_o is the $1/e^2$ radius (see Figure 6 and Table 1). These X-Y radii were then used to calculate the irradiances. This is called the direct CCD method.

For smaller beam spots (and the highest irradiance at $6x10^{17}$ W/cm^2), the CCD pixels were too large to resolve the spot; a target plate was then put into the focal plane, creating an image that was projected via a microscope (and enlarged) onto the CCD camera sensors and processed from there with the Beamgage software. This is called the microscope method.

Estimated uncertainty for radial spot size was 10% for the direct CCD method (runs # 11-16, 19 and 5-6) and 50% for the microscope method (run #25).

From the spot size measurements, another factor was also determined and considered to estimate the irradiance onto the target surface: the laser energy fraction within a 2σ radius of the spot size (100% for all irradiances, except 34% at $6x10^{17}$ W/cm^2).

Target

For each run, a target was positioned at the chamber center. The target included a plate of gold (thin 0.01 mm and thick 0.1 mm), copper (1 mm thick), or polyimide (*i.e.*, 0.125 mm Kapton HN). The target could be moved by an XYZ motor (see Figure 5) such that the target front face was positioned at the focus and the laser beam of a fixed irradiance can be rastered over the target front surface (to ensure a fresh target surface for every laser pulse). The laser-target angle was always 90 degrees for the selected runs, but some runs were also taken with a 45° angle.

Accurate positioning of the target at the focal plane for each run was performed by adjusting the location of the CCD camera in the focused beam such that the spot size was smallest. This defined the focal plane. Then camera was swapped with the target, with taking the finite thickness of the target into account. The positioning the target was believed to be within 10 μm from the focal plane, which is less than or comparable to the Raleigh length of the focal spot.

Challenges

A number of challenges prevented this experiment from consistently achieving irradiances more than about $1x10^{17}$ W/cm^2:

1. Damage of the final focusing optic due to coating from the target ablation plume (this effect was huge for the Kapton target and large for all other targets at high irradiances). For example, Figure 7 shows how an OAP mirror's surface was damaged after a series of shots on Kapton and Au targets. Such damage reduced the mirror's reflectivity and consequently the laser energy to the target. From frequent reflectivity measurements, an average reflectivity was determined for each run, and from that the average energy (and average irradiance) in each run. Focal spot characterization was also necessary each time a focusing optic was replaced due to damage or for changing irradiance.

2. Alignment of focusing optics with short focal length. Such optics is sensitive to aberrations. In particular, the alignment of OAP mirrors was very difficult, which resulted in larger uncertainties for high irradiances.
3. Precise positioning of target at focal plane was difficult due to the small Rayleigh range of short focal length optics.
4. Flexing of the target foils as damage to the surface occurs could move the target out of the focal plane.
5. Beam alignment was sensitive to the target chamber flexing during vacuum cycling, opening/closing chamber doors, *etc.*

Table 1: Summary of laser, optic and target parameters for the runs with good quality.

Run #	11-16	19	5-6	25
Energy before Compressor (mJ)	212 (5%)	221 (5%)	210 (5%)	220 (5%)
Ratio after/before Compressor	0.65 (8%)			
Reflectivity of Focusing Mirror (before and after the run)	1.0 to 1.0	0.95 to 0.5	0.95 to 0.6	0.87 to 0.37
Energy Fraction within 2σ	1	1	1	0.34
Average Laser Energy onto Target (mJ)	138 (9%)	104 (31%)	106 (27%)	30 (65%)
Pulse Length FWHM (fs)	55 (27%)			
Peak Power (W)	2.5×10^{12} (28%)	1.9×10^{12} (40%)	1.9×10^{12} (38%)	5.5×10^{11} (70%)
Focusing Mirror	Spherical Mirror	OAP	OAP	OAP
Measured Spot Size $1/e^2$ Radius (Horizontal and Vertical in μm)	67 x 79	56 x 41	35 x 35	10 x 6
Laser-Target Angle	90-degree	90-degree	90-degree	90-degree
Target	0.1 & 0.01 mm Au	0.1 mm Au	0.1&0.01 mm Au	1 mm Cu
Laser time on target	48 min	8.2 min	20 min	18.7 min
Irradiance on Target (W/cm^2)	3.0×10^{16}	5.2×10^{16}	1.0×10^{17}	6×10^{17}
Irradiance Total Uncertainty	30%	40%	40%	85%

1) 0.8 μm laser wavelength.
2) Percentage values in parenthesis are relative uncertainties in one standard deviation.
3) Estimated uncertainty for radial spot size was 10% for the direct CCD method (runs # 11-16, 19 and 5-6) and 50% for the microscope method (run #25).

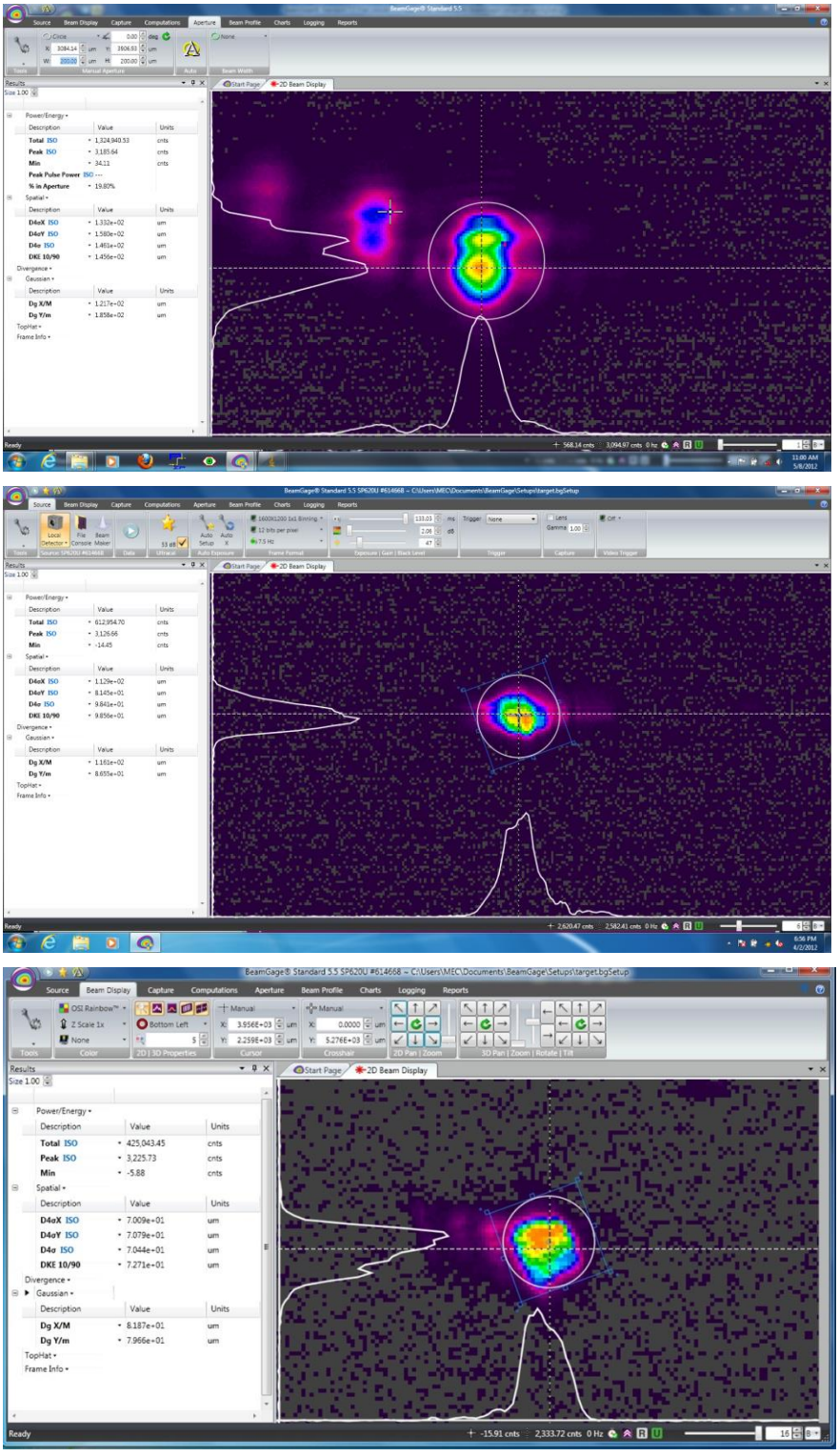

Figure 6: CCD measurements of focal spot size (4σX and 4σY diameters), which gave X-Y radius of 67x79 μm, 56x41 μm, and 35x35 μm for the irradiance of 3.0×10^{16}, 5.2×10^{16} and 1.0×10^{17} W/cm^2, respectively (from top to bottom).

Achieved Irradiations

Table 1 summarizes the laser, optic and target parameters for the 10 runs at the four irradiance levels of $3.0x10^{16}$, $5.2x10^{16}$, $1.0x10^{17}$ and $6x10^{17}$ W/cm^2. The main uncertainties for the measurements of laser and optic parameters were associated with the OAP reflectivity (due to surface damage) and the focal spot size determination for irradiance > $1x10^{17}$ W/cm^2. The total uncertainty (one standard deviation) for the irradiance was estimated to be about 40% at lower irradiances and 85% for the highest irradiance at $6x10^{17}$ W/cm^2.

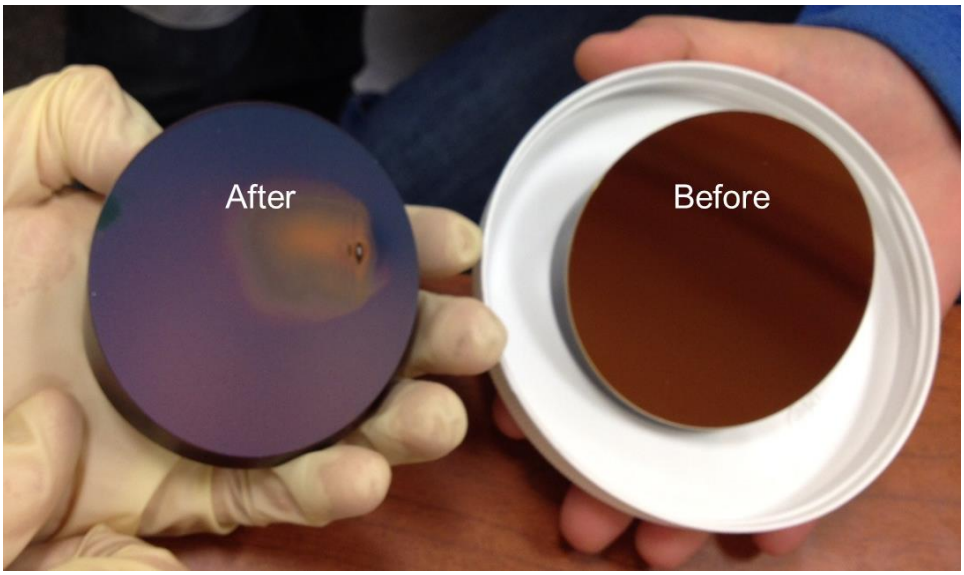

Figure 7: An Off-Axis Parabolic (OAP) mirror was damaged after a series of laser shots on Kapton and Au.

Post-run Target Examination

The target plates were examined using a microscope after the runs to check the pattern and spacing of damage sites. Figure 8 shows the 0.1-mm and 0.01-mm gold foils with rastered shot pattern and the microscope examination of the 0.1-mm Au foil damaged after shots at $1x10^{17}$ W/cm^2. The bottom figure shows the copper target after several runs at $6x10^{17}$ W/cm^2. The raster spacing was found to be large enough to avoid overlapping ablated areas, the ablated sizes were uniform and consistent with beam size measurements.

Each laser shot was able to punch through the gold foil, but not through the 1-mm copper (except in one run, where rastering was turned off to keep the laser pulses on the same location to see how not having a fresh target surface might affect the radiation yield).

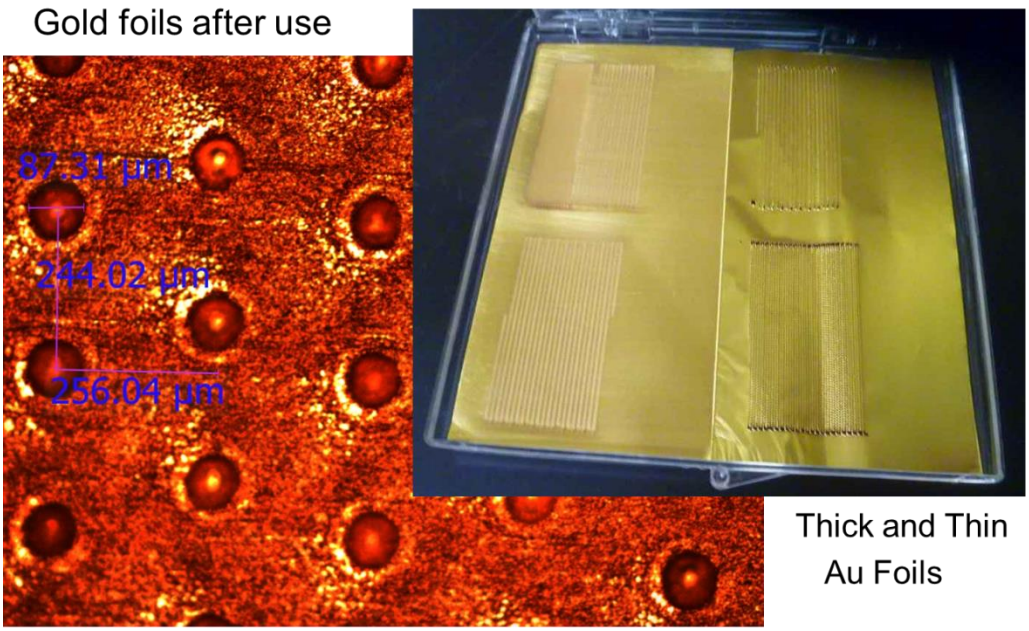

Figure 8: Target with raster laser shot pattern. TOP: 0.1-mm and 0.01-mm gold foils and the microscope examination of the damaged 0.1-mm Au foil from shots at $1x10^{17}$ W/cm^2. BOTTOM: 1-mm copper target from several runs at $6x10^{17}$ W/cm^2.

Summary of RPD Model for Photon Dose Calculations

This section summarizes the RPD model for photon dose calculations [5,6]. The photon yield from laser on target interaction is determined by several parameters: the laser energy per pulse, the fraction of the laser energy converted into the energy of the hot electrons, the electron spectrum, and the efficiency of conversion from electrons to bremsstrahlung photons.

The photon dose per laser pulse is a strong function of laser irradiance, is linearly proportional to the laser energy per pulse, but does not depend strongly on the atomic number of target material. The photon dose rate is linearly proportional to the laser repetition rate.

The fraction of the laser energy converted into the energy of the hot electrons (conversion efficiency) used in the RPD model was 30% for laser irradiance $\leq 10^{19}$ W/cm^2 and 50% above 10^{19} W/cm^2.

Electron Spectrum and Electron Temperature

The Maxwellian distribution shown in Eq. 5 was used to describe the hot electron spectrum generated from laser with intensity $\leq 10^{18}$ W/cm^2 hitting a solid target:

$$f(E) = E^{1/2} e^{-E/T} / T^{3/2} \qquad (5)$$

where E is the electron energy and T is the electron temperature.

For solid targets, the electron temperature, T (keV), for the electron spectrum is defined as a function of the normalized irradiance ($I\lambda^2$), which is the product of the laser irradiance, I (W/cm^2), and the square of the laser wavelength, λ (μm).

When $I\lambda^2 < 1.6\text{x}10^{17}$ W/cm^{2}μm^2, the inverse bremsstrahlung and resonance absorption are the dominant mechanisms for producing hot electrons, and Eq. 6 is used to calculate the electron temperature T (keV):

$$T \approx 6\times10^{-5} \left[I\lambda^2\right]^{1/3} \qquad (6)$$

When $I\lambda^2 \geq 1.6\text{x}10^{17}$ W/cm^{2}μm^2, the ponderomotive force theory applies, and Eq. 7 is used to calculate the electron temperature T (keV):

$$T = M_e(\sqrt{1.0 + I\lambda^2 / 1.37\times10^{18}} - 1) \qquad (7)$$

where M_e is the electron rest mass (511 keV).

Figure 9 shows the electron temperature predicted from Eqs. 6 and 7 as a function of irradiance with an inflection point at $2.5\text{x}10^{17}$ W/cm^2 (for a laser wavelength of 0.8 μm), where the switch from Eq. (6) to Eq. (7) occurs. See Table 2 for sample values of electron temperature.

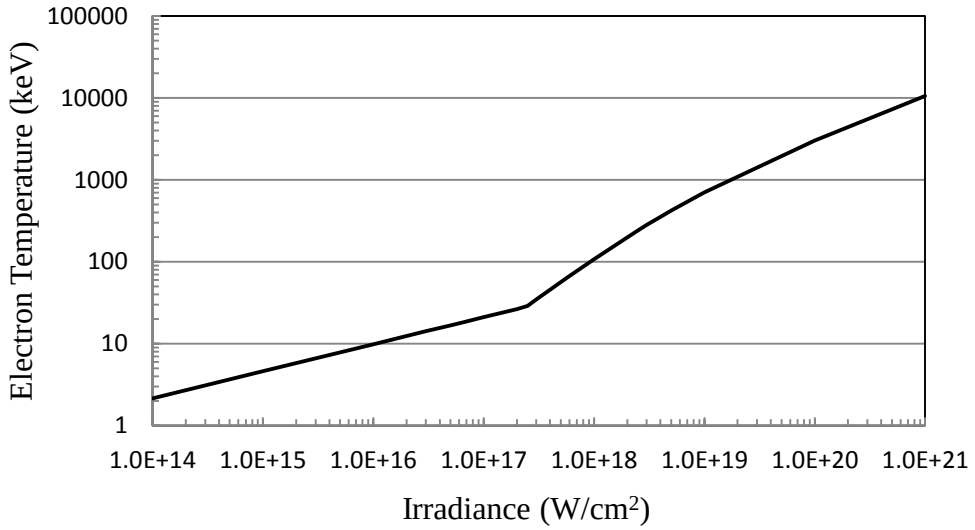

Figure 9: Electron temperature as a function of irradiance with an inflection point at $2.5x10^{17}$ W/cm^2 (laser wavelength of 0.8 μm), predicted using Eqs. 6 and 7.

Table 2: Photon dose yield (mSv/J) and dose rate (150 mJ per pulse at 10 Hz) at 1 m for laser (0.8 μm wavelength, 40 fs pulse length) hitting a solid target, based on RPD model

Irradiance (W/cm^2)	**Electron Temperature (keV)**	**Dose Yield without shielding (mSv/J)**	**Dose Yield with 5-mm glass shielding (mSv/J)**	**Dose Rate with 5-mm glass shielding at 150 mJ per pulse and 10 Hz (mSv/h)**
10^{14}	2.2	2.8×10^{-7}	1.9×10^{-9}	1.0×10^{-5}
10^{15}	4.6	1.3×10^{-6}	5.1×10^{-8}	2.8×10^{-4}
10^{16}	10	5.8×10^{-6}	6.9×10^{-7}	3.7×10^{-3}
10^{17}	21	2.6×10^{-5}	5.8×10^{-6}	3.1×10^{-2}
2.5×10^{17}	29	5.0×10^{-5}	1.4×10^{-5}	7.6×10^{-2}
5×10^{17}	57	1.9×10^{-4}	7.6×10^{-5}	0.41
10^{18}	108	6.9×10^{-4}	3.7×10^{-4}	2.0
10^{19}	706	3.0×10^{-2}	2.4×10^{-2}	1.3×10^{2}
10^{20}	3019	0.90	0.83	4.5×10^{3}
10^{21}	10545	3.2	3.1	1.7×10^{4}

Photon Dose Calculations

In theory, the photon dose can be calculated using Monte Carlo codes using the estimated conversion efficiency of laser energy to electron energy, the electron spectrum, and the

bremsstrahlung process in the target. However, this is difficult to do as the actual energy, angular and spatial distributions of the hot electrons are not known.

Y. Hayashi *et al.* [9] derived equations to estimate the 0-degree photon dose generated through the interaction between a short high-power laser pulse and a solid target. The equations were based on an electron spectrum with the Relativistic Maxwellian distribution [$\propto E^2 \exp(-E/T)$] at higher irradiance and the maximum 0-degree bremsstrahlung dose formula proposed by Swanson in IAEA-188 [10] for estimating the forward-peaked photon dose. A constant of 1.8 was applied to correct for the photon dose difference between the analytic estimation and EGS4 Monte Carlo calculations. The final equations to estimate the 0-degree photon dose are given in Eq. 8 [5,9]:

$$\begin{aligned} H_x &\approx 1.8 \times (1.10 \times P_{ef.} / R^2) \times T^2 \qquad (T < 3MeV) \\ H_x &\approx 1.8 \times (3.32 \times P_{ef.} / R^2) \times T \qquad (T \geq 3MeV) \end{aligned} \tag{8}$$

where H_x is the normalized photon dose in Sv/J, P_{ef} is the laser to electron energy conversion efficiency, R is the distance from the target to measurement point in cm, and T is the electron temperature in MeV. Beyond an electron temperature of 3 MeV (~1x10^{20} W/cm^2 at 0.8 μm), most electrons are of high energies, and the normalized photon dose is reaching saturation.

Equation 8 was developed for the high irradiance range ($I\lambda^2$ from 10^{19} to 10^{21} μm^{2}W/cm^2) considering only the ponderomotive force theory [9]. The RPD photon dose model uses Eq. 8 with the above-mentioned conversion efficiencies, as well as Eqs. 6 and 7 for estimations of the electron temperature, for all intensity range. Table 2 lists the photon dose yield obtained from the RPD model for various irradiances, all at 1 m from a solid target with and without 5-mm-glass shielding.

The angular distribution of hot electrons may not be isotropic, depending on the energies of hot electrons and the target self-shielding. The RPD model estimates the maximum 0-degree bremsstrahlung dose per Eq. 8, which may result in an overestimation for the photon doses at other angles, depending on the laser intensity and target conditions.

Photon Spectrum for Shielding Calculations

For the purpose of shielding calculations, the bremsstrahlung photon spectrum in Eq. 9 for intensity ≤ 10^{18} W/cm^2 is used in the RPD model:

$$N_p(E_p) = C \frac{1}{E_p} \exp(-\frac{E_p}{T}) \tag{9}$$

where E_p is the photon energy, T is the electron temperature, and C is a constant.

The bremsstrahlung spectrum in Eq. 9 is consistent with the Maxwellian distribution of electrons in Eq. 5, when a bremsstrahlung yield spectrum of E_p^{-1} (thin target) or E_p^{-2} (thick target) is used. The constant C should satisfy that the integration of the energy of all the photons equates to the product of the laser pulse energy and the laser energy to X-ray energy conversion efficiency. Therefore, the constant C is dependent on the electron temperature, the laser pulse energy, and

the laser to X-ray energy conversion efficiency. Because the absolute photon dose is calculated using Eq. 8, the constant *C* does not need to be determined for the relative dose calculation of shielding.

In air, focusing is limited by the air ionization threshold of ~5x10^{14} W/cm^2. This ensures that higher irradiances cannot be reached in air, and radiation hazard from laser-target interaction only occurs in vacuum. Therefore, a 5-mm-thick glass view port was used to calculate the minimum shielding effect of the MEC target chamber for a photon spectrum described in Eq. 9 using FLUKA for irradiances between 10^{14} and 10^{20} W/cm^2 [5,6]. The material of the glass was assumed as Borosilicate (Pyrex) with a density of 2.23 g/cm^3. The shielding effects for the MEC 2.54 cm Al chamber wall and three common LCLS hutch materials (*e.g.*, 1.21 mm steel roll-up door, 0.79 mm lead-lined side wall, and 10.16 cm concrete roof) were also calculated for irradiances between 10^{17} and 10^{18} W/cm^2.

Figure 10 shows the calculated attenuation factors of ambient dose equivalent for the shielding materials described above. Note that the cases of steel, lead and concrete shielding are for a photon spectrum that is already hardened by 5 mm glass. Another case of 1.21 mm steel following the 2.54-cm Al shielding is also shown to further illustrate the spectrum-hardening effect. When the laser irradiance gets lower, the attenuation becomes higher because the electron temperature gets lower and then the photon spectrum becomes softer and easier to shield. The attenuation results for 5 mm glass and 2.54 cm Al are relevant to the interpretation of the MEC radiation measurement results outside the target chamber (see section below). The attenuation results for the two cases of 1.21 mm steel are relevant to the MEC radiation measurements outside the equipment roll-up door.

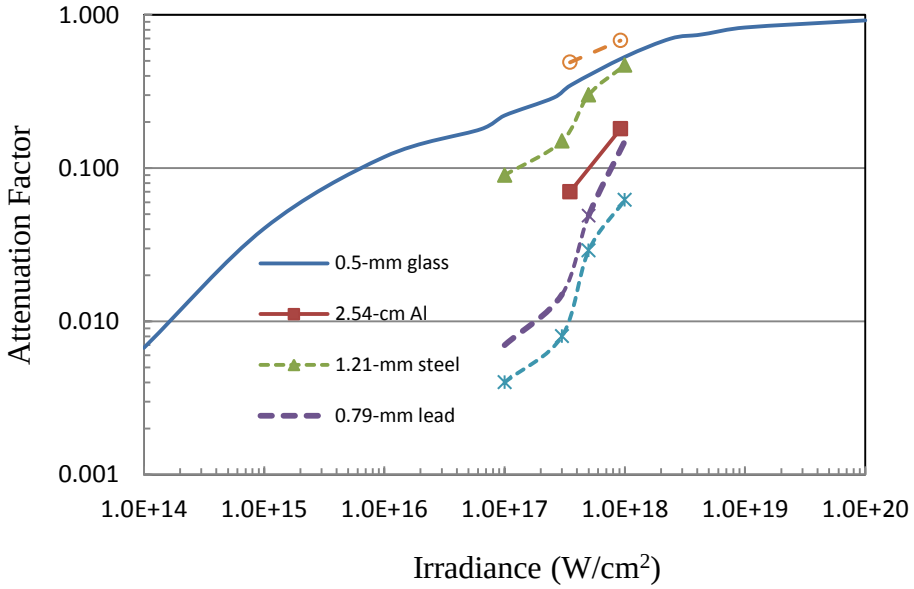

Figure 10: Attenuation factors of ambient dose equivalent for five shielding materials, calculated with FLUKA using the photon spectrum of Eq. 9. The cases of steel, lead and concrete are for spectra already hardened by 5 mm glass or 2.54 cm Al.

Radiation Measurements

This section describes the radiation measurement results using various types of passive and active detectors inside and outside of the MEC Al-wall target chamber as well as outside the MEC lead-lined hutch wall and steel equipment door at different irradiance values. Comparison between measurements at four irradiance levels ($3.0x10^{16}$, $5.2x10^{16}$, $1.0x10^{17}$ and $6x10^{17}$ W/cm^2) and the photon dose estimations from the PRD model is also given.

Detector Types and Locations

Figure 11 shows the measurement locations and types of passive detectors placed around the MEC target chamber. Figure 12 shows the measurement locations and types of active detectors placed around the MEC target chamber. The radius of the chamber is about 1 m, and the Al wall is typically 2.54 cm thick. The target was set at 90 or 45 degrees relative to the laser beam direction, but the 10 runs with good results had angle at 90-degree such that the locations #1, #7 and #16 were in the "backward" direction. Figure 13 illustrates the passive and active detectors outside the MEC target chamber.

Figure 13 also shows the detector layout at two backward locations at mid-plane: a dosimeter set inside a blue basket and a Victoreen 451B survey meter at location #7, as well as a set of soup-cup-like HPI-6031, blue PTW-7262, HPI-6032 and Victoreen 451B detectors at location #8. The positioning of active instruments may have had a self-shielding effect on the responses of the PTW-7262 and HPI-6032 detectors.

<u>Passive dosimeters</u>

These dosimeters include:

- electronic dosimeters (Rados RAD-60),
- pocket ion chambers (PICs with full scale at 2 mR or 200 mR), and
- personnel dosimeters (Landauer Luxel+, Inlight, and Panasonic models).

The dosimeters were placed inside 18 small blue plastic baskets (generally one Rados, two 2-mR PICs, one 100-mR PIC, and two per type of personnel dosimeter in each basket) on the chamber wall (about 1.2 m from the target). See Table 3 for where these dosimeters were located with respect to the beam height, and which shielding they were behind.

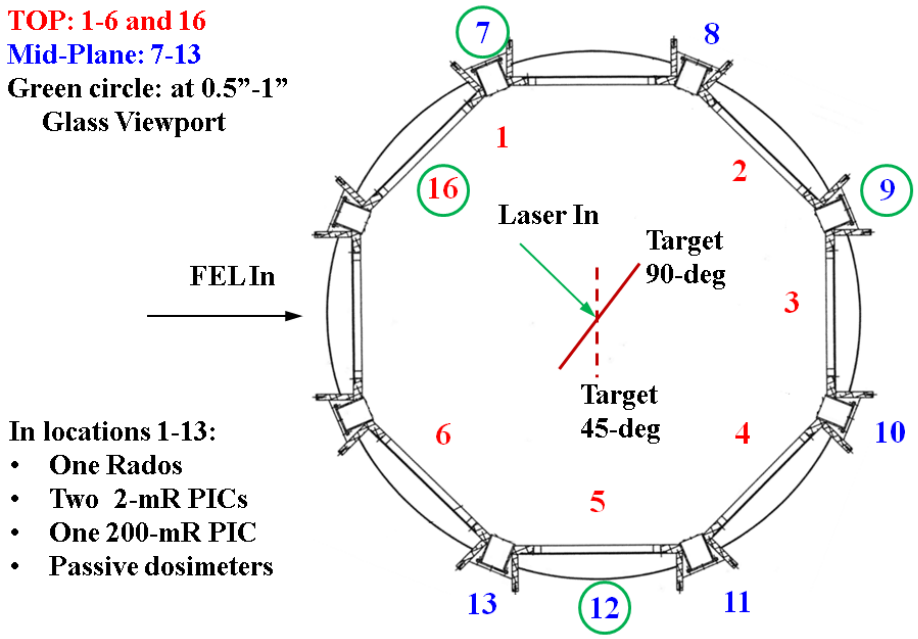

Figure 11: Locations and types of passive detectors (incl. RADOS) placed around the MEC target chamber. Not shown are the locations at the bottom, since the thick aluminum bottom of the chamber shielded these dosimeters so well that no radiation was detected there.

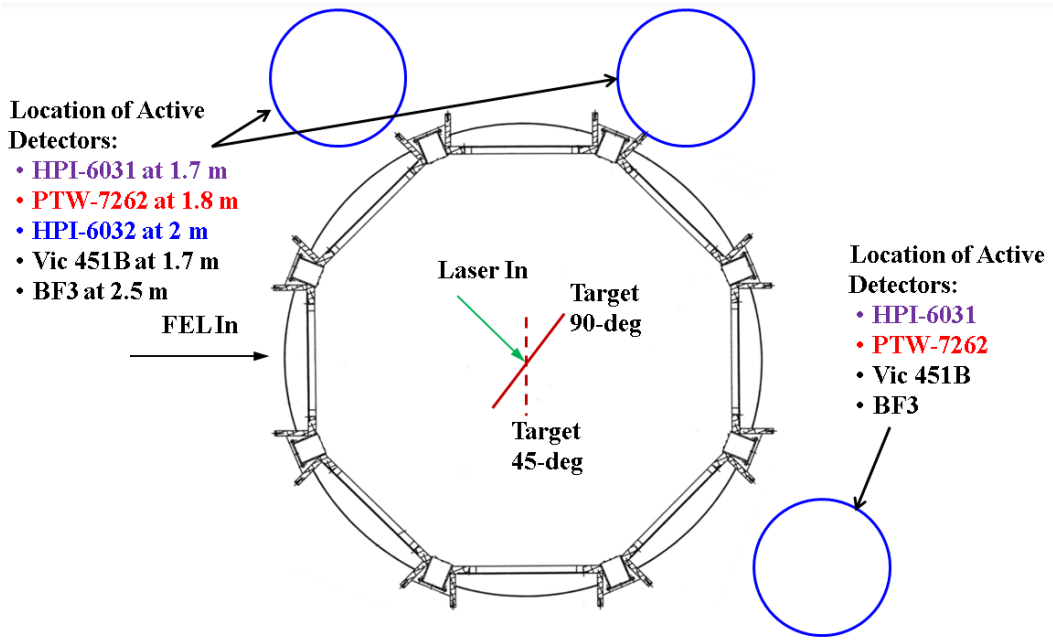

Figure 12: Locations and types of active detectors placed around the MEC target chamber. The set on the top was always at one of the two indicated locations.

Figure 13: TOP - detectors (including two BF_3 stations) outside the MEC target chamber. BOTTOM - detector layout at a backward location showing a set of dosimeters inside a blue basket and a Victoreen 451B survey meter, as well as the set of HPI Soup Cup detectors.

Table 3: Location (position number) of dosimeter sets (PICs, Rados, personnel dosimeters) right outside the target chamber. Refer also to Figure 11.

	Shielding in Front of Dosimeter Set		
	Glass		**Aluminum**
	1.27 cm	**2.54 cm**	**1.9 cm**
Top of Chamber	16		1, 2, 3, 4, 5, 6
Beam Height	7, 9	12	8, 10, 11, 13

Active Photon Detectors

For real-time monitoring, three types of active photon instruments were placed at the locations #10 and #7 (or initially #8 for run #5-6):

- two HPI-6031 thin-walled air ion chambers at 1.7 m from the target,
- two PTW-7262 pressurized argon ion chambers behind the HPI-6031 chamber at 1.8 m from the target, and
- one HPI-6032 Al-walled ion chamber behind the PTW-7262 chamber at 2 m from the target.

Active Neutron Detectors

Two SLAC-made neutron detectors (a BF_3 probe with 5"-radius polyethylene moderator) were used to measure neutron doses at locations #8 and #10 (2.5 m from the target).

Victoreen Ion Chambers at Chamber

Three Victoreen 451B ion chamber survey meters were placed in mid-plane at locations #7, #8 and #10, about 1.7 m from the target, to measure photon doses in integration mode for each run.

Victoreen Ion Chambers outside Hutch

A Victoreen 451B meter was placed on the MEC equipment roll-up door (5 m from the target), the weakest shielding of Hutch 6, to monitor photon radiation outside the hutch in real time.

Dosimeters inside Target Chamber

Figure 14 shows the placement of eight sets of paired Landauer NanoDot dosimeters inside the target chamber at 8 locations (30 cm from the target) as well as a gold foil target at the chamber center. These dosimeters were exchanged several times during the experiment.

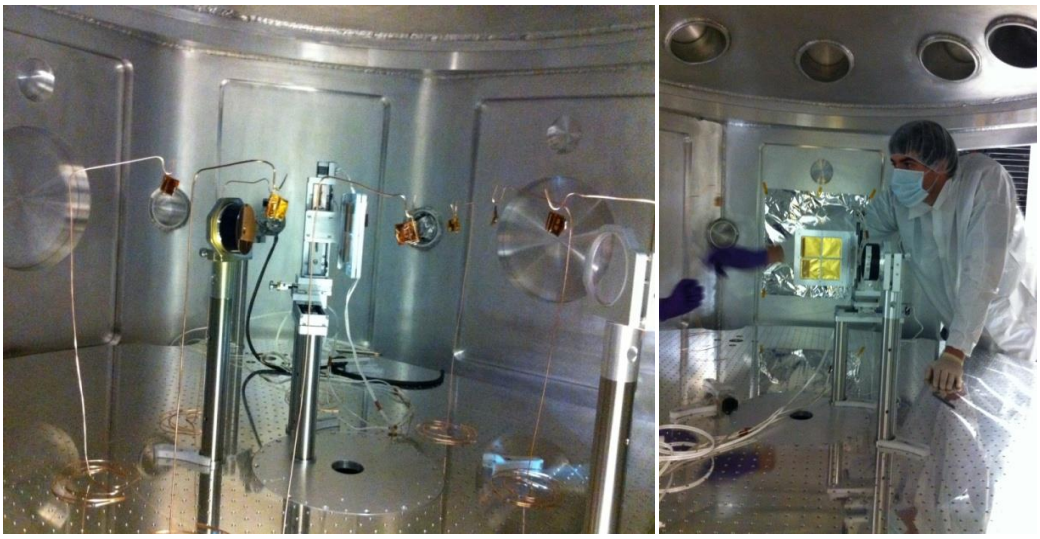

Figure 14: LEFT - placement of 8 sets of paired Landauer NanoDot dosimeters inside target chamber at 30 cm from the target. The dosimeters were wrapped into Kapton tape and hung from copper wire stands. RIGHT - a gold foil target was placed at the chamber center.

Passive Dosimeters outside Target Chamber and Hutch

Total photon doses over all runs outside target chamber were measured by paired InLight dosimeters at locations #1 to #13. Several sets of paired Landauer Inlight dosimeters were also placed on the outer sides of the MEC hutch walls (0.8 mm or 1.6 mm lead lined) and equipment roll-up door (1.2 mm steel) to monitor the integrated doses over all runs.

Spot Surveys

Spot surveys with the Victoreen 451B/451P meters were conducted outside the hutch wall during the laser shots.

Detector Properties

Table 4 summarizes the detection limits and signal reporting frequencies for the detectors. The PICs with 200 mR scale and personnel dosimeters have high detection limits (5-10 mrem) and were useful only for measurements at very high irradiance. The more sensitive PICs (those with 2-mR scale) and Rados have low detection limits (0.05 and 0.1 mrem, respectively). It was found that the integrated doses for most runs were small and below the detection limits of the 200-mR PICs and personnel dosimeters. In the section below, the integrated doses reported by dosimeters outside the chamber for each run are from the Rados and 2-mR PICs.

The Victoreen 451B survey meter can be operated in rate or integration mode (detection limit of 0.1 μR). The pressured PTW-7262 detector is very sensitive (detection limit of 0.001 mrem/h), but has a thick steel wall that makes its response not sensitive to photons < 80 keV. The HPI-6032 detector is a modified version of the HPI-6030 detector, which utilizes the model 1055 Chipmunk ion chamber (detection limit of 0.01 mrem/h). On the other hand, the HPI-6031 detector has a higher detection limit of 0.1 mrem/h, but its thin plastic wall makes it sensitive to photons down to 10 keV.

Table 4: The detection limits and signal reporting frequency for detectors.

Detector Type	**Detection Limit**	**Reporting Frequency**
Pocket Ion Chamber (PIC; 2-mR scale)	0.05 mrem	integration
Electronic Dosimeter (Rados)	0.1 mrem	integration
Personnel Dosimeter (InLight and Panasonic)	5 mrem	integration
Landauer NanoDot Dosimeters	1 mrem	integration
Victoreen 451B Air Ion Chamber Survey Meter	0.1 μR, 7 keV	1s or Integration
PTW-7262 Ion Chamber	0.001 mrem/h	0.5 s
HPI-6032 Ion Chamber	0.01 mrem/h	1 s
HPI-6031 Ion Chamber	0.1 mrem/h	60 s
SLAC-made Moderated BF_3 Neutron Detector	0.5 μrem/h	1 min

The SLAC-made moderated BF_3 detector can detect neutrons down to 0.5 µrem/h with an energy response similar to that of a traditional Anderson-Braun remmeter. Fast neutron dose rates were estimated from the total moderated BF_3 signals using a conversion factor of 800 counts/µrem for neutrons with an average energy of 1 MeV.

The PTW-7262 and HPI-6032 detectors have a fast response and signal reporting frequency (0.5 s and 1 s, respectively). The HPI-6031 detector used for the measurements has a long signal reporting frequency of 60 seconds, which gives the dose rate averaged over every 60 s. This response difference can be seen clearly in the figures below.

Figure 15 shows the real-time readouts of PTW and HPI detectors for one the runs. The continuous and remote radiation monitoring feature of PTW and HPI detectors was also a useful tool for diagnosis for possible optic and target conditions.

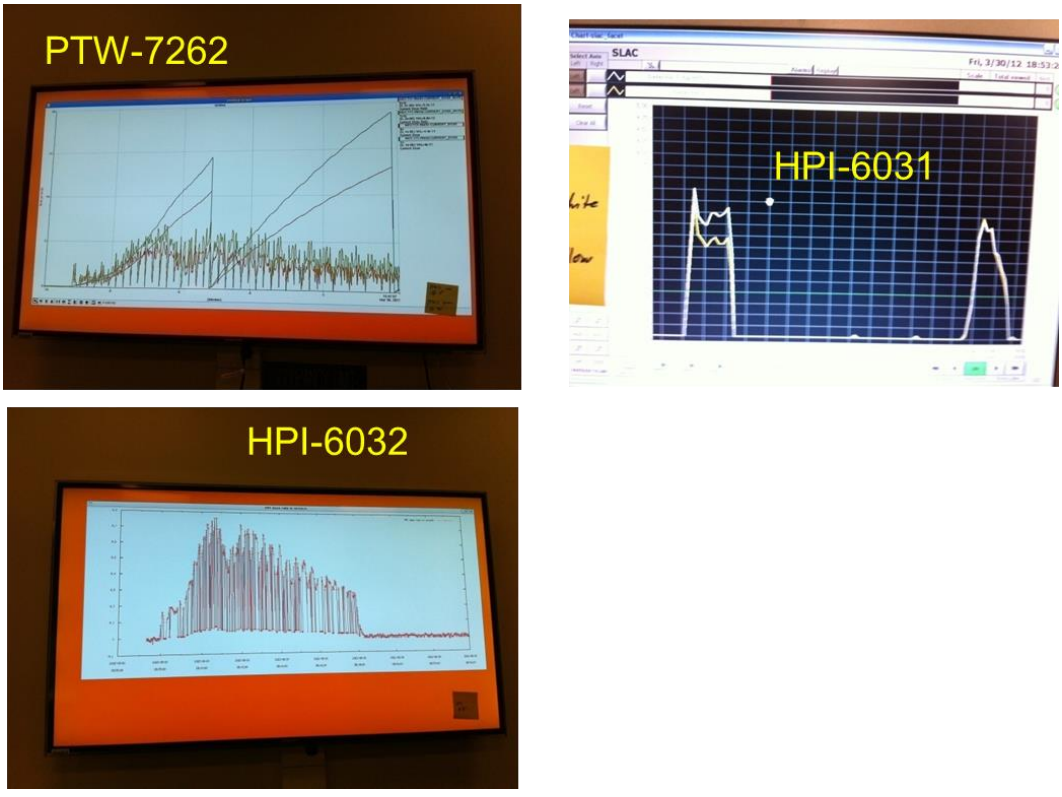

Figure 15: Remote and continuous readouts of three types of active photon detectors (two PTW-7262, one HPI-6032 and two HPI-6031) for one of the runs. Note the difference in the response and signal reporting frequency.

Radiation Measurement Results

The radiation environment depends on the laser irradiance and laser energy. Inside the target chamber, electrons are expected to dominate the radiation environment. Because of the viewports and thick Al chamber wall (a few cm), only bremsstrahlung photons from electrons hitting the target itself or the chamber wall are expected outside the target chamber. Exceptions are the photons passing through the glass viewports, since they tend to have higher intensities and in the average lower energies than those outside the Al chamber wall.

Active Instruments

Figures 16 to 18 show the real-time dose rate results. At 3.0×10^{16} W/cm^2, the dose rates were too small to be measured by the PTW and HPI detectors. The radiation spikes in the fast-response PTW and HPI-6032 detectors were caused by alignment changes during the laser-target rastering. Slowly decreasing radiation level by a factor of ~2 at higher-intensity runs were due to mirror degradation. Because of these two effects, the average dose rate over the run was used for the PTW and HPI detectors.

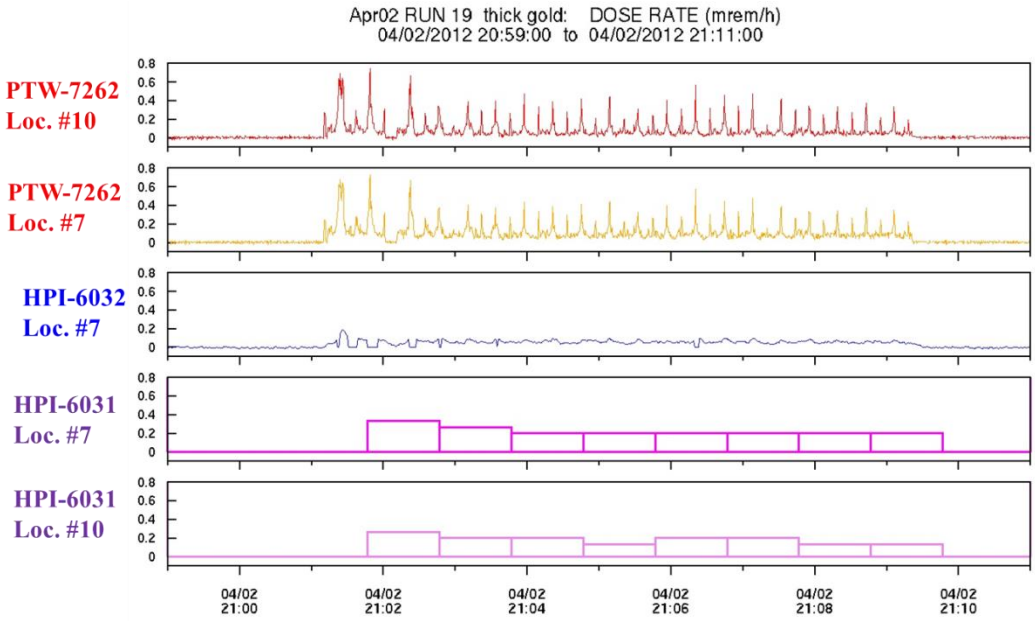

Figure 16: Dose rate (mrem/h) measurement results for PTWs and HPIs for Run #19 (5.2×10^{16} W/cm^2 on 0.1-mm gold for 8.2 minutes).

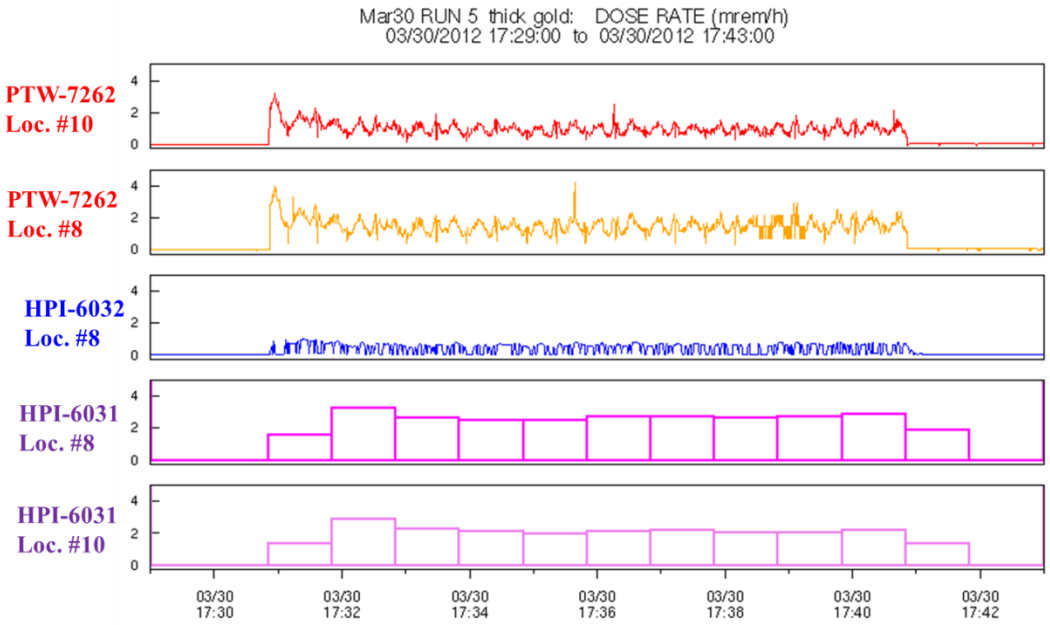

Figure 17: Dose rate (mrem/h) measurement results for PTWs and HPIs for Run #5 ($1.0x10^{17}$ W/cm^2 on 0.1-mm gold for 10 minutes).

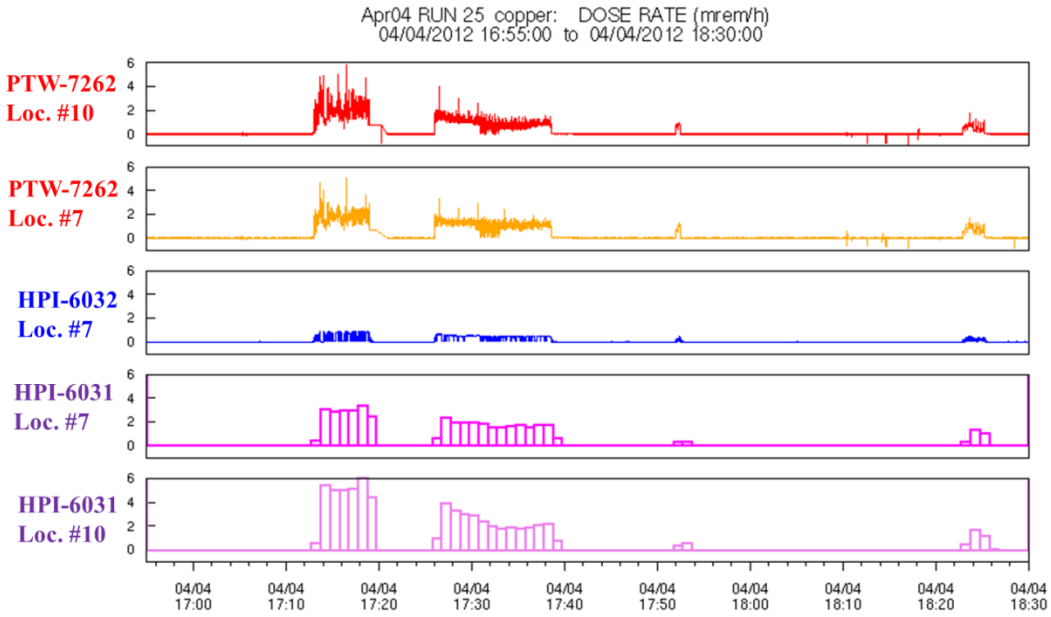

Figure 18: Dose rate (mrem/h) measurement results for PTWs and HPIs for Run #25 ($6x10^{17}$ W/cm^2 on 1-mm copper for 18.7 minutes).

Dosimeters inside Target Chamber

Figures 19 to 22 summarize the very high doses (rad in tissue) from low-energy electrons measured by the eight paired Landauer NanoDot dosimeters inside the target chamber. The backward direction had much higher dose than the forward direction (maximum dose at about 180°). The maximal doses and corresponding electron dose rates are listed in Table 5. For example, for run #19 (5.2×10^{16} W/cm^2 on 0.1-mm gold), the maximum dose was 203 rad for 8.2 minutes and 104 mJ at 30 cm, the electron dose rate 190 rad/h at 1 m, 150 mJ and 10 Hz.

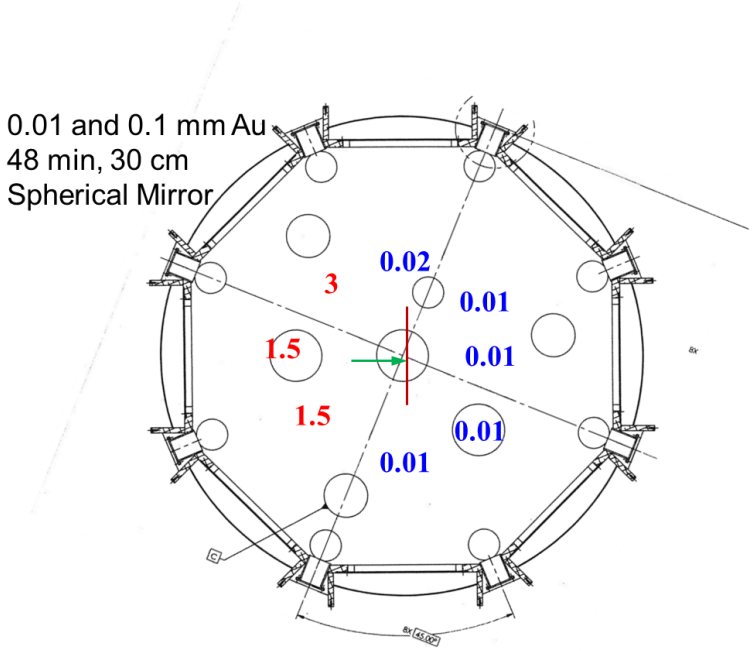

Figure 19: High doses (rad in tissue) from low-energy electrons measured by eight NanoDot dosimeters inside the target chamber at 30 cm from the target (runs #11-16: 3.0×10^{16} W/cm^2 and 138 mJ).

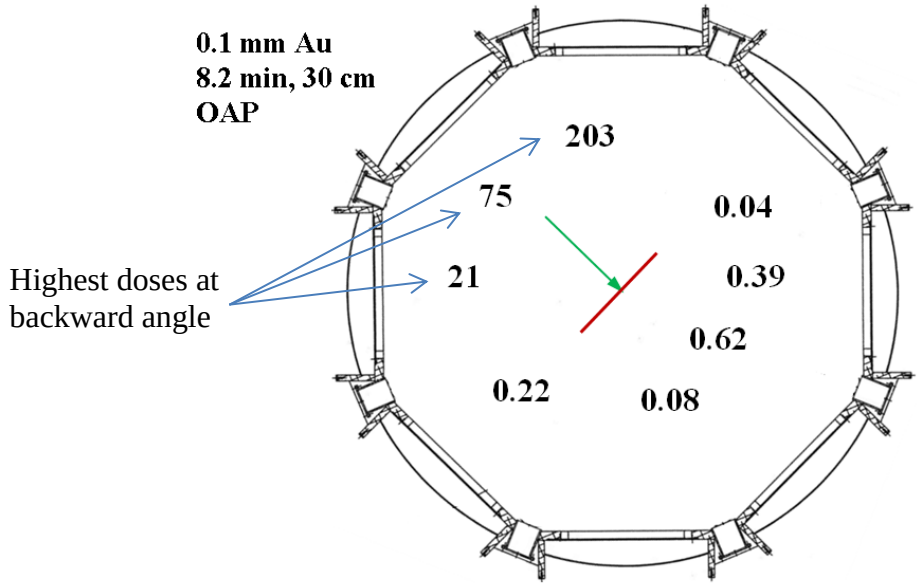

Figure 20: Results from NanoDot dosimeters inside the target chamber: High doses (rad in tissue) from low-energy electrons at 30 cm from the target (run #19: 5.2×10^{16} W/cm^2 and 104 mJ).

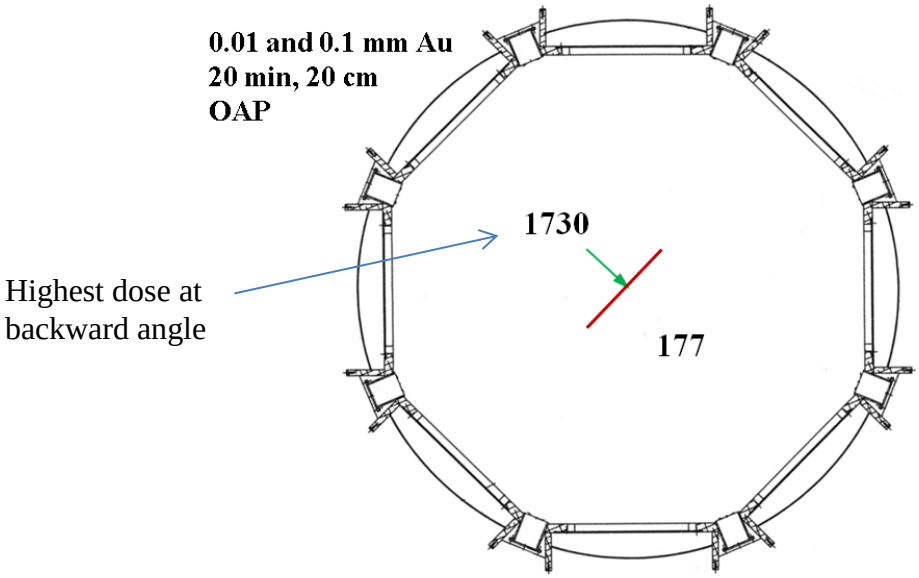

Figure 21: Results from NanoDot dosimeters inside the target chamber: High doses (rad in tissue) from low-energy electrons at 20 cm from the target (runs #5-6: 1.0×10^{17} W/cm^2 and 106 mJ).

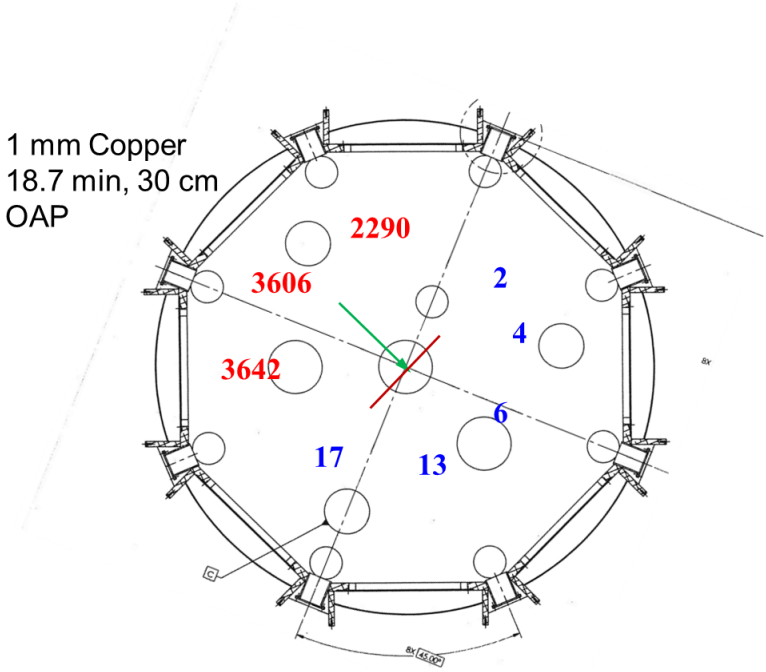

Figure 22: Results from NanoDot dosimeters inside target chamber: High doses (rad in tissue) from low-energy electrons measured at 30 cm from the target (run #25: $6x10^{17}$ W/cm^2 and 30 mJ).

Passive Dosimeters inside Hutch

Figures 23 to 26 summarize the photon doses (in mrem) measured outside the target chamber by passive and active dosimeters at various irradiances. The raw dose measurements were there converted dose rates using the length of the various runs. In general, the backward direction had slightly higher photon dose than the forward direction (by a factor of 2), and the maximum doses were measured by the Rados outside the glass view port on top of the chamber or by PIC/Rados at mid-plane at 180-degree.

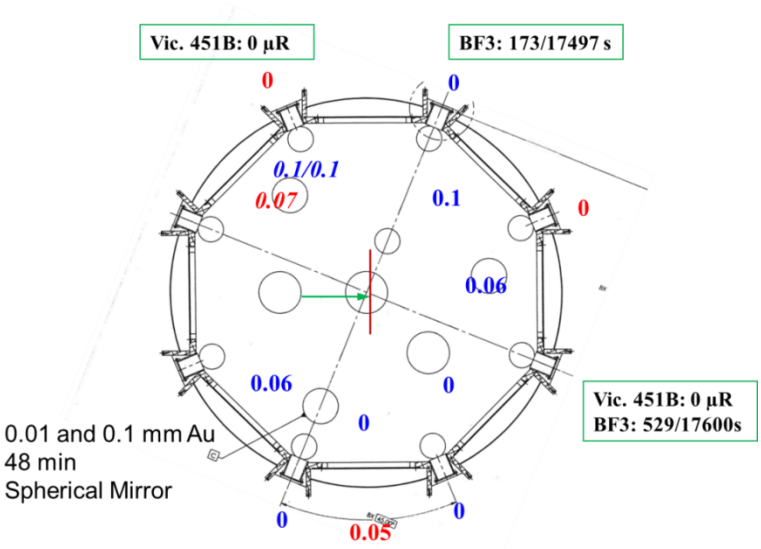

Figure 23: Integrated photon doses (mrem) measured by one Rados and Victoreen 451B meter (µR), as well as total BF_3 neutron counts, outside target chamber (runs #11-16: $3.0x10^{16}$ W/cm^2 and 138 mJ). Values in red were from glass viewports, in blue from ~1 inch aluminum.

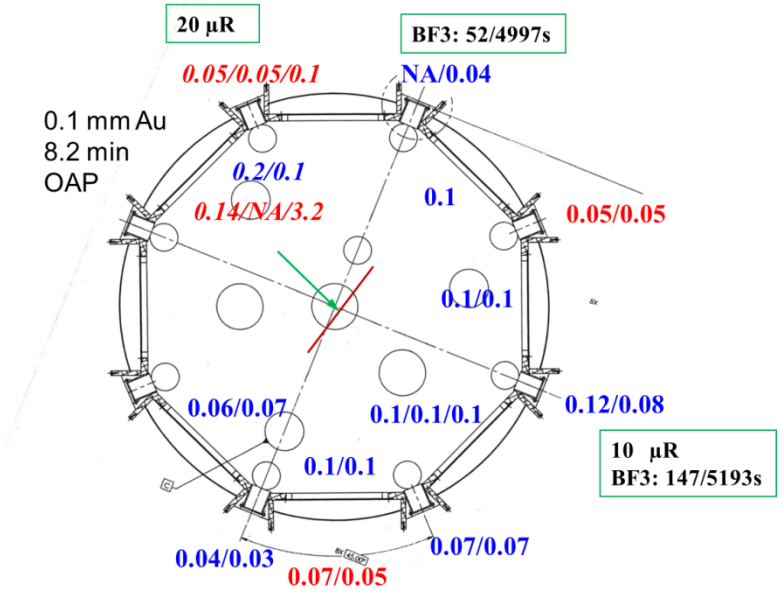

Figure 24: Integrated photon doses (mrem) measured by two PICs and one Rados at each location (the 3 numbers) and Victoreen 451B meter (µR), as well as total BF_3 neutron counts, outside target chamber (run #19: $5.2x10^{16}$ W/cm^2 and 104 mJ). Values in red were from glass viewports, in blue from ~1 inch aluminum.

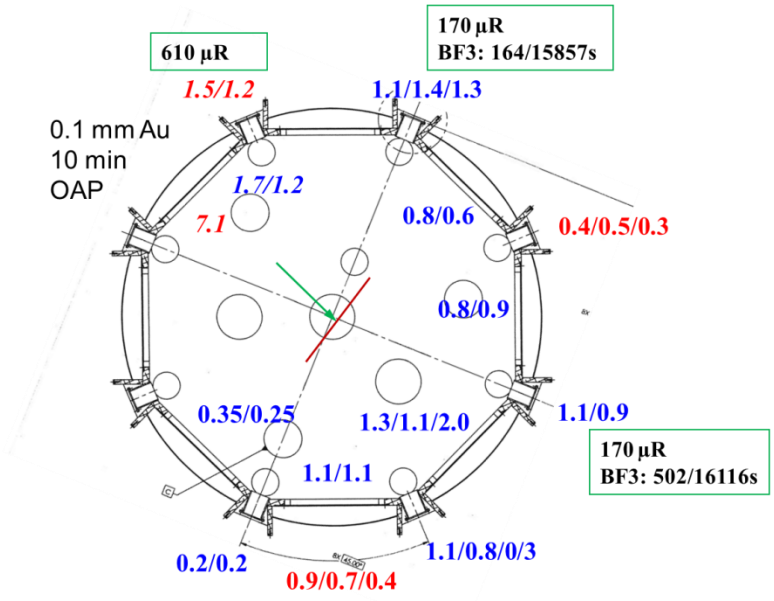

Figure 25: Integrated photon doses (mrem) measured by two PICs and one Rados at each location (the 3 numbers) and Victoreen 451B meter (µR), as well as total BF_3 neutron counts, outside target chamber (run #5: $1.0x10^{17}$ W/cm^2 and 106 mJ). Values in red were from glass viewports, in blue from ~1 inch aluminum.

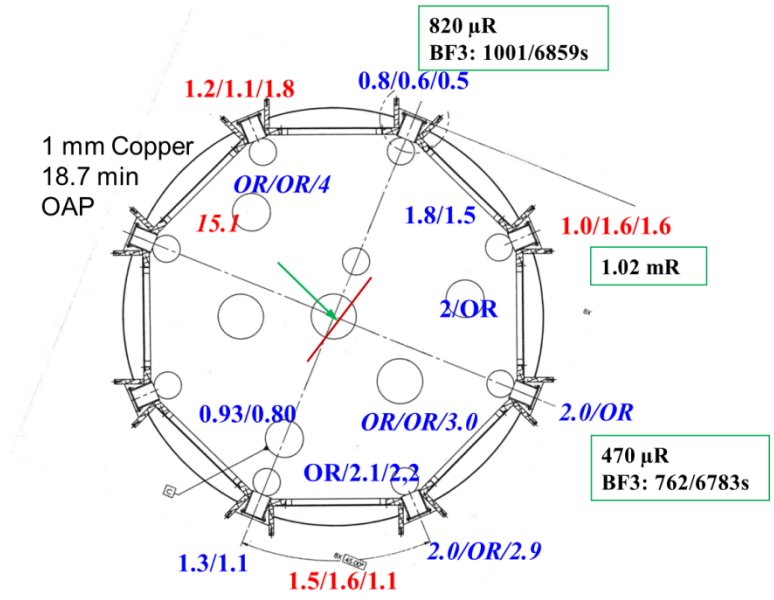

Figure 26: Integrated photon doses (mrem) measured by two PICs and one Rados at each location (the 3 numbers) and Victoreen 451B meter (µR), as well as total BF_3 neutron counts, outside target chamber (run #25: $6x10^{17}$ W/cm^2 and 30 mJ). "OR" stands for "over range."

Table 5 summarizes the photon dose results in Figures 16-18 for continuous monitoring (PTW-7262, HPI-6031, and HPI-6032), the electron doses measured inside chamber in Figures 19-22 (NanoDot dosimeters), and the photon doses outside target chamber in Figures 23-26 (Rados, 2-mR PIC and Victoreen 451B meter).

Note that the dose rates in Table 5 have all been normalized to 1 m from target and 150 mJ per pulse and 10 Hz. For comparison purpose, the photon dose rates estimated from the RPD model (mrem/h at 1 m and 150 mJ and 10 Hz with 5 mm glass shielding) using Eq. 8 are also given for the four irradiance values.

To illustrate shielding and directional effects, the results in Figures 23 to 26 are further categorized as PIC/Rados at mid-plane or on top of chamber (and outside glass viewport or Al blank flange). Though the electron doses inside chamber are anisotropic, the photon doses outside chamber are nearly isotropic. At the intensity levels, the shielding effect of Al chamber can be seen.

The four laser irradiance ($3.0x10^{16}$, $5.2x10^{16}$, $1.0x10^{17}$ and $6x10^{17}$ W/cm^2), average laser energy per run (mJ per pulse), and the electron temperatures (keV) calculated using Eqs. 6 and 7 are also shown.

Neutrons

The BF_3 detectors measured only background signals at three lower irradiances (about 0.6 and 1.8 cpm at locations #8 and #10, respectively) and, only at $6x10^{17}$ W/cm^2, it measured low-level neutrons of 0.12 and 0.07mrem/h at locations #8 and #10, respectively (at 1 m, 150 mJ and 10 Hz). This represents a neutron and photon dose ratio of about 0.2% at $6x10^{17}$ W/cm^2.

The neutron dose rate outside target chamber and the photon dose rate outside the equipment door are also shown in Table 5 for comparison.

Dose outside Hutch

Figure 27 shows that up to 0.2 mR/h was detected at $6x10^{17}$ W/cm^2 (run #25 with 1 mm copper target and run #26 with 0.1 mm Au) outside the 1.21 mm steel equipment door (5 m from target) with the Victoreen 451B survey meter in rate mode. Figure 10 shows that the attenuation factor of 1.21 mm steel at $6x10^{17}$ W/cm^2 is about 0.5. Therefore, 0.2 mR/h at 5 m and 30 mJ gives about 50 mrem/h outside target chamber (at 1 m and 150 mJ; 25 mrem/h if not considering steel shielding), which is consistent with those measured by PTW, HPIs, and Rados/PIC. This result (1 mrem/h at 5 m and 150 mJ) is important as it has implication to the annual dose to workers and users (dose limit of 100 mrem per year) who occupy the areas outside the MEC hutch.

Total Dose from Personnel Dosimeters

Figure 28 shows that the total photon doses for all runs (total beam-on time was 6.5 hours over 8 days) measured by the paired Landauer InLight dosimeters (detection limit of 5 mrem); the maximum was 41 mrem at the glass viewport (location #7), 6 to 23 mrem at mid-plane, and no doses outside hutch walls and roof. These doses were dominated by laser shots at high irradiances (see Figure 23 to Figure 26). These numbers are consistent with the sum of the doses from the individual runs.

Table 5: Summary of irradiance and dose measurement results.

Run #	11-16	19	5	25
Average Laser Irradiance (W/cm^2)	3.0×10^{16}	5.2×10^{16}	1.0×10^{17}	6×10^{17}
RPD Model Photon Dose Rate with 5-mm Glass Shielding (mrem/h at 1 m, 150 mJ and 10 Hz)	0.9	1.5	3.2	54
Max e- Dose inside Chamber at 30 cm from Target [rad/h in tissue at 1 m]	3 rad in 48 min [0.37]	203 rad in 8.2 min [190]	770 rad in 20 min [2] [290]	3642 rad in 18.7 min [5200]
Maximal Photon Dose Rate (mrem/h at 1 m, 150 mJ and 10 Hz)				
Vic 451B (#7, Al, Off-axis)	0	0.61	15.0	47
HPI-6031 (partially glass)	0	0.79	10.6	44
PTW-7262 (behind HPI-6031)	0	0.54	7.2	23
HPI-6032 (behind PTW, Al, Off-axis)	0	0.35	4.0	14
PIC/Rados (Mid-plane, Al)	0	1.8	17	67
PIC/Rados (Mid-plane, Glass)	0.1	1.5	18	41
PIC/Rados (Top, Al, #1)	0.14	2.2	15	66
Rados (Top, Glass, #16)	0.14	49	87	347
Average Photon Dose Rate (exclude Rados at Top, Glass, #16)	**0.03**	**1.1**	**12**	**43**
Ratio between RPD Model and Average Dose Rate	30	1.4	0.3	1.3
Photon Dose Rate outside Steel Roll-up Door by Vic. 451B (mrem/h at 5 m and 150 mJ)	0	0	0	1.0
Neutron Dose Rate by BF_3 (mrem/h) [Neutron/Photon Ratio in %] [3]	0	0	0	0.09 [~0.2%]

1) Unless otherwise stated, dose rates are normalized to 1 m from target and 150 mJ per pulse and 10 Hz.
2) Total dose for run 5 (10 min on 0.1-mm Au) and run 6 (10 min on 0.01-mm Au) at same irradiance, corrected to 30 cm.
3) A conversion factor of 800 counts/μrem for moderated BF_3 detector for fast neutrons with average energy of 1 MeV was used. The BF_3 detector measured only background signals at three lower irradiances.

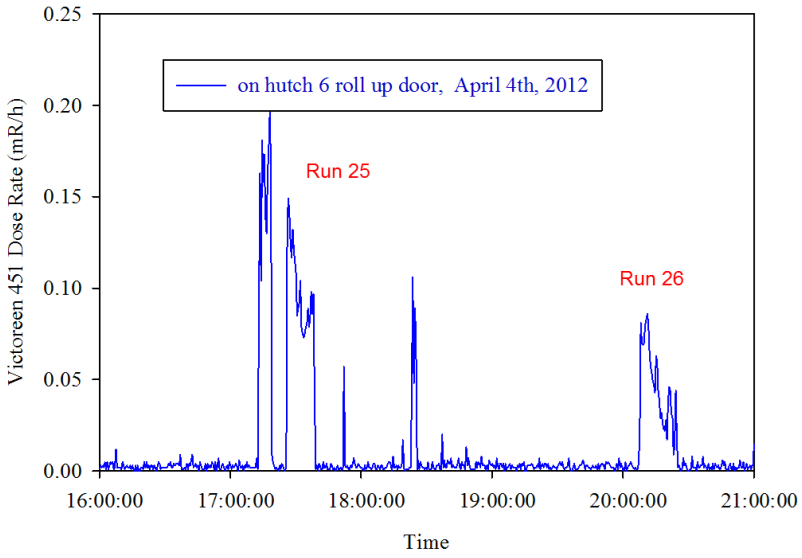

Figure 27: Photon dose rate measured on the steel roll-up door (about 5 m from target) with the Victoreen 451B survey meter for run #25 (max. 0.2 mR/h; $6x10^{17}$ W/cm^2 on 1-mm copper) and run #26 (max. 0.08 mR/h; $6x10^{17}$ W/cm^2 on 0.1-mm gold), both at average laser energy of 30 mJ over the runs.

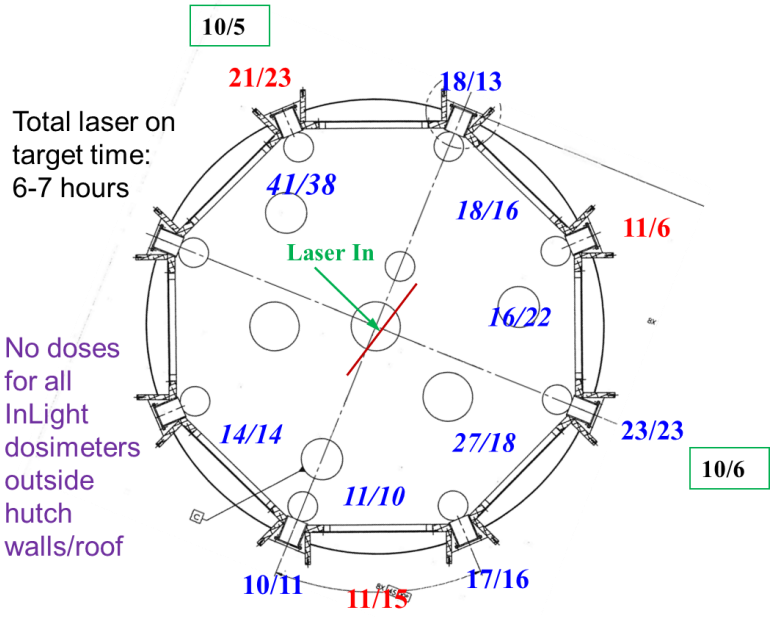

Figure 28: Total photon doses (mrem) measured by paired InLight dosimeters for all runs.

Photon Dose versus Laser Irradiance

Figure 29 summarizes the measured results in terms of photon dose yield (mSv/J at 1 m) outside MEC target chamber and compares them with those calculated with RPD model. Figure 30 summarizes the measured results in terms of photon dose rates (normalized to 150 mJ per shot and 10 Hz), which can be compared easily with Table 5.

Figures 29 and 30 show that the photon dose measured by active and passive detectors were consistent among different types of detectors, except the Rados on top of the chamber (the glass view port at location #16) which recorded higher dose rates (a factor of 5 at higher irradiances). The PTW-7262 and HPI-6032 detectors consistently recorded lower dose rates by a factor of 2-3 when compared to other detectors, a result likely due to the self-shielding from detector positioning (see Figure 13) and their thicker detector walls.

Considering the large uncertainties in the irradiance measurements, the measurements agree well with the calculations at $1.0x10^{17}$ and $6x10^{17}$ W/cm^2. They are lower than the calculations at $3.0x10^{16}$ and $5.2x10^{16}$ W/cm^2, likely because the RPD model only assumes the minimal attenuation by 5 mm glass). The RPD model gives the reflection point at $2.5x10^{17}$ W/cm^2 such that the dose is linearly proportional to the irradiance below the reflection point and is proportional to the square of the irradiance above the reflection point, and then become linear at irradiance $>1x10^{20}$ W/cm^2.

For completeness, Figure 31 compares the photon doses (mSv/J at 1 m) calculated by the RPD model covering the whole range of 10^{15} and 10^{21} W/cm^2 (with and without 5-mm-glass viewport shielding) with the RP measurements outside MEC target chamber from10^{16} to 10^{18} W/cm^2. In addition, the following 3 measurements at irradiances > 10^{19} W/cm^2 are also included [7,11,12] in the figure:

1. The RP measurements outside the LLNL Titan chamber ($1x10^{20}$ to $6x10^{20}$ W/cm^2, 1.053 μm laser wavelength, 0.7-1 ps, 50-400 J per pulse, a few mg/cm^2 of hydrocarbon foam followed by 1-mm-gold target, 1.5"-thick Al target chamber),
2. The measurement results at Vulcan [11] ($4x10^{19}$ to $4x10^{20}$ W/cm^2, 1 ps, ~230 J per pulse, a few mm Au, Cu, or Al targets, 2-cm-thick Al target chamber), and
3. At LULI [12] ($1x10^{19}$ to $3x10^{19}$ W/cm^2, 1.057 μm laser wavelength, 300 fs, 5-20 J per pulse, < 1-mm-thick Au, Al or teflon targets, 1-cm-thick steel target chamber).

Figure 31 shows that at irradiances < 10^{17} W/cm^2, where electron temperature is low and photon spectrum can be attenuated easily by target chamber wall (a factor of 5 even by 5-mm-glass), measurements tend to give much lower doses than the RPD model, which assumes minimum shielding. At irradiances of 10^{17} - 10^{19} W/cm^2, the RPD model gives a reasonable estimation of photon dose. At irradiances > 10^{19} W/cm^2, the RPD model gives an estimate that is conservative by a factor of 3-5.

Figure 32 compares the photon dose yield (mSv/J at 1 m without shielding) calculated by the RPD model with the measurements of electron doses at MEC (maximum at 180-degree and minimum at 0-degree) and the neutron doses measured at MEC and LULI [11]; the latter is ~1% of the LULI measured photon doses (also shown).

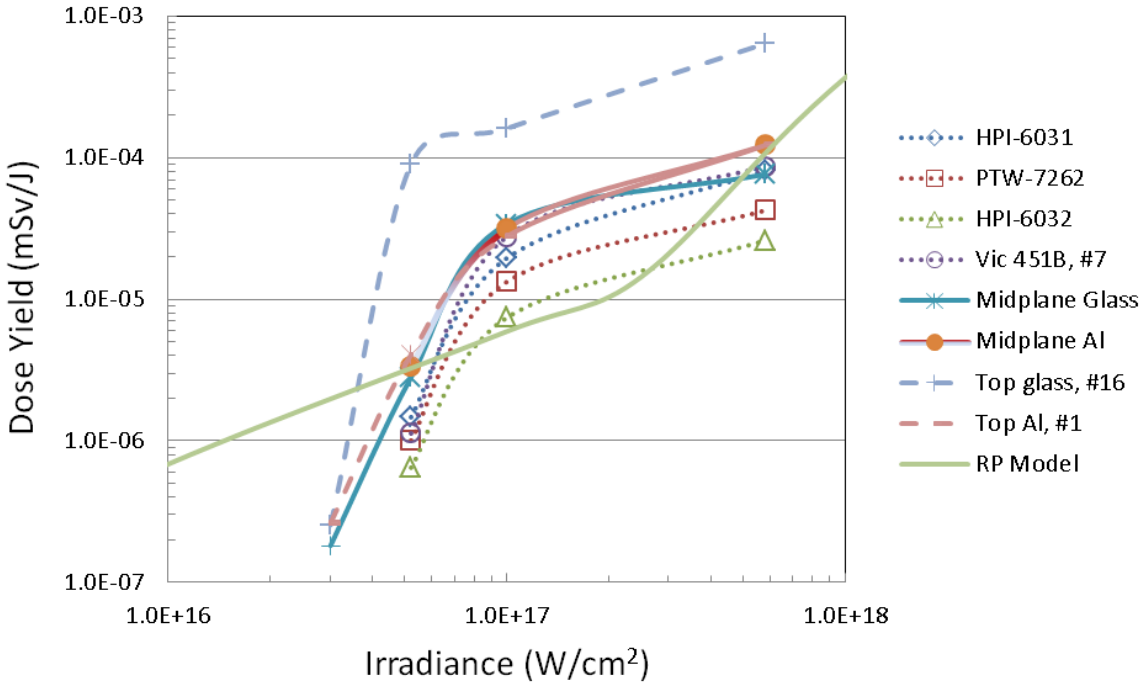

Figure 29: Comparison between the measured photon dose yield (mSv/J at 1 m) outside target chamber with those calculated with RPD model with 5-mm glass.

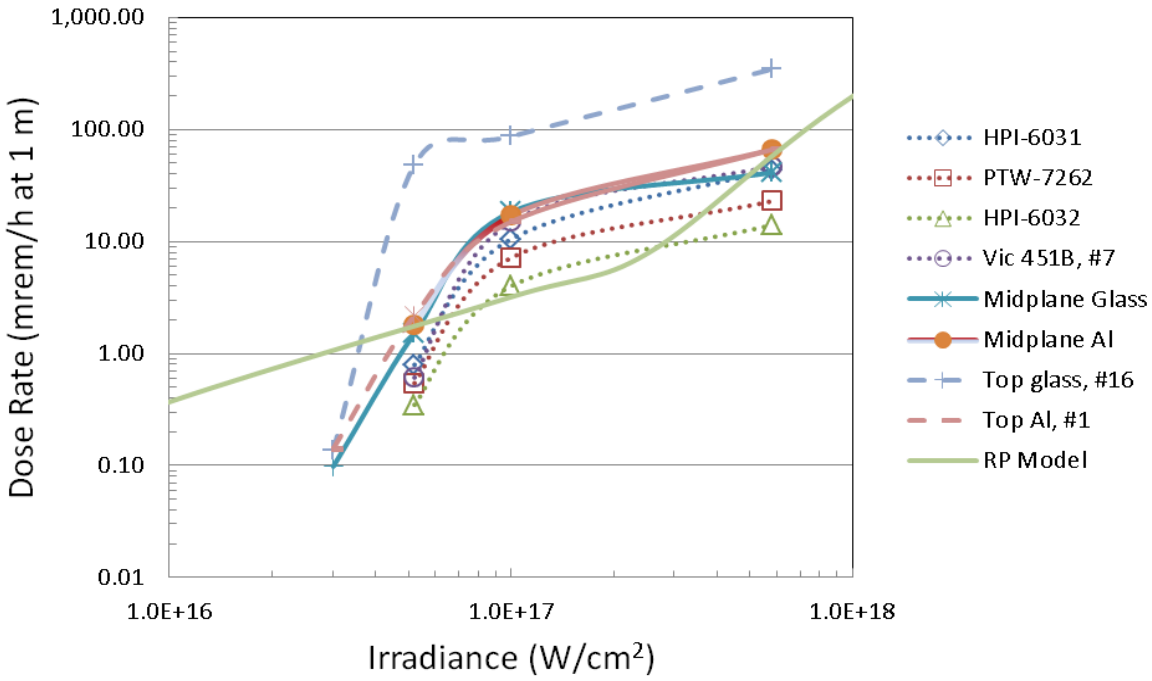

Figure 30: Comparison between the measured photon dose rates (mrem/h at 1 m) outside target chamber with those calculated with RPD model with 5-mm glass (normalized to 150 mJ and 10 Hz).

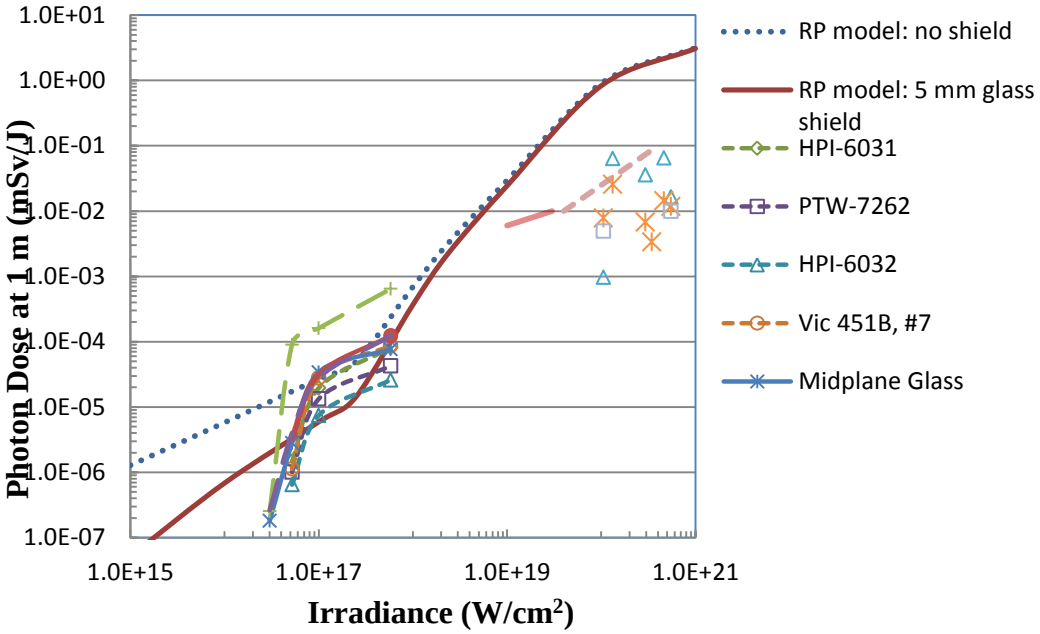

Figure 31: Comparison between the photon dose yield (mSv/J at 1 m) calculated by the RPD model from 10^{15} and 10^{21} W/cm^2 (with and without 5-mm-glass viewport shielding) with the measurements: RP measurements outside MEC target chamber from10^{16} to 10^{18} W/cm^2, the RP measurements outside the LLNL Titan chamber (1×10^{20} to 6×10^{20} W/cm^2), and the published measurement results at Vulcan (4×10^{19} to 4×10^{20} W/cm^2) and LULI (1×10^{19} to 3×10^{19} W/cm^2).

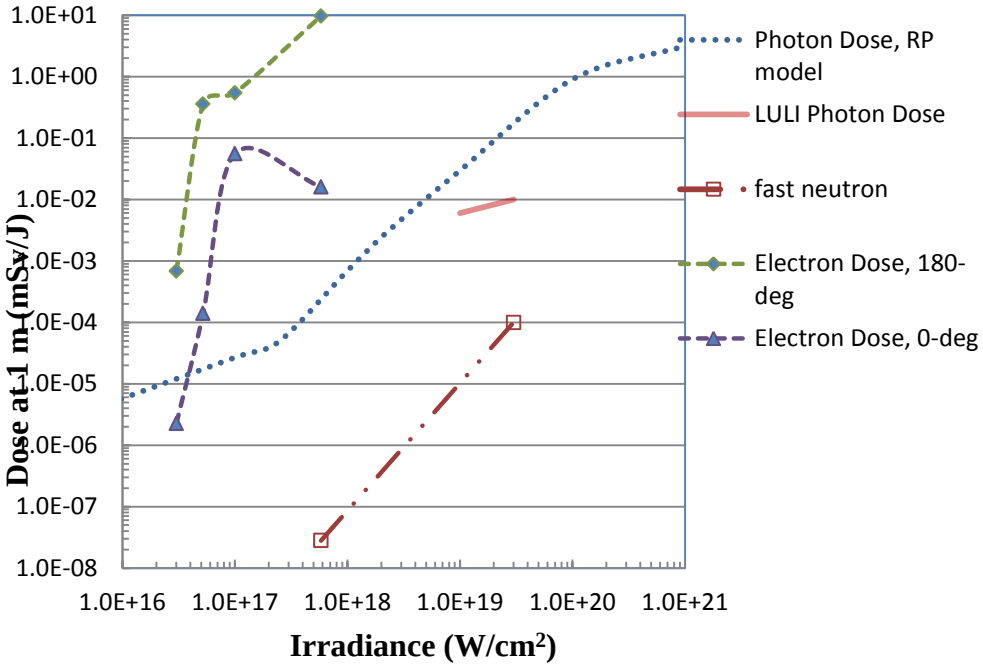

Figure 32: Comparison between the photon dose yield (mSv/J at 1 m without shielding) calculated by the RPD model with the measurements of electron doses (MEC 180-deg and 0-deg) and neutron doses (MEC and LULI).

Conclusions

Ionizing radiation measurements from high-intensity laser-induced plasma interactions on solid targets inside the Al-walled vacuum chamber of the LCLS MEC instrument were conducted using passive and active detectors at irradiance between $3x10^{16}$ and $6x10^{17}$ W/cm^2.

Each run of the more than 20 runs had a unique set of laser, optic and target conditions with laser pulses rastering over the target surface mainly perpendicularly at a fixed irradiance. Significant effort was made in characterizing the laser irradiance values for each configuration of laser, focusing mirror, and target; four irradiances with targets of Au foils and copper plate were found to produce good measurement results.

At the measured irradiance range of 10^{16} and 10^{18} W/cm^2, the dependence of photon dose on the type of target (Au, copper or plastic) or laser incidence angle (90 or 45 degrees), if any, could not be observed from this experiment. Electron doses inside the target chamber were highly anisotropic and peaked at backward direction by several orders of magnitude. Photon doses outside the target chamber were nearly isotropic (a factor of ~2 higher in backward direction).

The measured photon dose rates at 1 m (150 mJ and 10 Hz) outside the target chamber (when averaged over different types of detectors) 6 were in good agreement with the calculated values of the RPD model (with 5 mm glass shielding), except at $3.0x10^{16}$ W/cm^2, which has an electron temperature of only 14 keV.

When considering the large uncertainties of the irradiance (a factor of 2-3) and the potential shielding effects from detectors and target chamber, the measured photon doses were in good agreement with those calculated with the RPD dose model. The RPD model predicts reasonable dose results that can be used for hazard analysis at the range of 10^{16} to 10^{18} W/cm^2. On the other hand, the RPD model gives a conservative estimate of the published dose results at irradiance > $1x10^{19}$ W/cm^2. The dose yield scales roughly with both laser irradiance and laser energy, particularly at irradiance >10^{19} W/cm^2.

At $6x10^{17}$ W/cm^2, a low level of ~0.1 mrem/h from fast neutrons was measured (at 1 m, 150 mJ and 10 Hz) with a neutron-to-photon dose ratio of 0.2%. This is equivalent to a neutron dose yield of $2.8x10^{-8}$ mSv/J (to be compared to the LULI measurements of $1x10^{-4}$ mSv/J at $3x10^{19}$ W/cm^2). The neutron yield may have shielding implications particularly at very high irradiances.

Both active and passive types of detectors performed well and the dose results were consistent, which is the same as the dose measurements in the LLNL Titan laser facility. Active detectors were not affected by the electromagnetic pulses associated with the MEC laser system; this was different from the Titan radiation measurements, in which all active detectors (Rados, Victoreen 450 P/B and 451 P/B meters, and Meridian neutron remmeter) failed to respond, likely due to the high EMP in the Titan's high laser intensity fields.

References

[1] S. C. Wilks and W. L. Kruer, "Absorption of ultrashort, ultra-intense laser light by solids and overdense plasmas", IEEE Journal of Quantum Electronics, 33 (11): 1954-1968 (1997).

[2] T. Guo *et al.*, "Generation of hard x rays by ultrafast terawatt lasers", Review of Scientific Instruments, 72 (1): 41-47 (2001).

[3] L. M. Chen *et al.*, "Study of hard x-ray emission from intense femtosecond Ti-sapphire laser-solid target interactions", Physics of Plasmas, 11(9): 4439-4445 (2004).

[4] H. Chen *et al.*, "Hot electron energy distributions from ultraintense laser solid interactions", Physics of Plasmas, 16, 020705:1-4 (2009).

[5] R. Qiu *et al.*, "Preliminary radiation hazard analysis of X-ray generated by high intensity laser systems", SLAC RP Note RP-10-11, November 2010.

[6] R. Qiu *et al.*, "Analysis and mitigation of X-ray hazard generated from high intensity laser-target interaction", SLAC-PUB-14351, January 2011.

[7] J. Bauer, J. C. Liu, A. A. Prinz, H. Tran, and Z. Xia, "High intensity laser induced radiation measurements at LLNL", SLAC RP Note RP-11-11, December 2011.

[8] M. Woods, "Laser beam focusing and propagation", SLAC LSO Memo 2010-10, October 2010.

[9] Y. Hayashi *et al.*, "Estimation of photon dose generated by a short pulse high power laser", Radiation Protection Dosimetry, 121(2): 99-107 (2006).

[10] W. Swanson, "Radiological Safety Aspects of the Operation of Electron Linear Accelerators," IAEA-188, 1979.

[11] R. J. Clarke *et al.*, "Radiological characterization of photon radiation from ultra-high-intensity laser-plasma and nuclear interaction", Journal of Radiological Protection, 26, p277-286 (2006).

[12] F. Borne *et al.*, "Radiation protection for an ultra-high intensity laser", Radiation Protection Dosimetry, 102(1): 61-70 (2002).

Acknowledgements

Other than the authors, many other people contributed to and/or supported the planning, preparation and conduct of experiments and post-experimental tasks: I. Evans, M. Welch, W. White, RP staff (J. Allan, E. McGee, L. Nicholas, S. Xiao, RPFO technicians and RP Dosimetry staff) and D. Rodgers from LBNL.

This work was supported by Department of Energy contract DE-AC02-76-SFO0515.